



LES investigation of cavitating flows around a sphere with special emphasis on the cavitation–vortex interactions

Yun Long^{1,2} · Xinping Long^{1,2} · Bin Ji¹

Received: 5 July 2020 / Revised: 24 August 2020 / Accepted: 8 September 2020 / Published online: 19 October 2020
© The Chinese Society of Theoretical and Applied Mechanics and Springer-Verlag GmbH Germany, part of Springer Nature 2020

Abstract

Large eddy simulation (LES) was coupled with a homogeneous cavitation model to study turbulent cavitating flows around a sphere. The simulations are in good agreement with available experimental data and the simulated accuracy has been evaluated using the LES verification and validation method. Various cavitation numbers are simulated to study important flow characteristics in the sphere wake, e.g. periodic cavity growth/contraction, interactions between the cloud and sheet cavitations and the vortex structure evolution. The spectral characteristics of the wake for typical cloud cavitation conditions were classified as the periodic cavitation mode, high Strouhal number mode and low Strouhal number mode. Main frequency distributions in the wake were analyzed and different dominant flow structures were identified for each of the three modes. Further, the cavitation and vortex relationship was also studied, which is an important issue associated with complex cavitating sphere wakes. Three types of cavitating vortex structures alternate, which indicates that three different cavity shedding regimes may exist in the wake. Analysis of vorticity transport equation shows a significant vorticity increase at the cavitation closure region and in the vortex cavitation region. This study provides a physical perspective to further understand the flow mechanisms in cavitating sphere wakes.

Keywords Cavitation · Cavitating flow · Sphere · Large eddy simulation (LES) · Vortex structure

1 Introduction

Cavitation is a complex two-phase flow phenomenon that frequently occurs in hydraulic machinery when the liquid pressure decreases to below the saturation vapor pressure [1]. The harmful effects of cavitation are very common, such as vibration, noise, material erosion and performance reductions in hydraulic machinery [2]. Cloud cavitation has been an important part of cavitation research for a long time due to the unknown inner flow details and complex flow mechanisms. Brandner et al. [3] and De Graaf et al. [4] conducted extensive experimental studies of cavitation behind spheres and observed numerous cavitation phenomena on the sphere including the formation, shedding and collapse of sheet cavitation

and even the occurrence of supercavitation. Many complex vortex structures were observed during cloud cavitation in the sphere wake. However, limited experimental data is available and many interesting phenomena in sphere wakes have not been well studied. This motivates a large eddy simulation (LES) investigation of sphere wake characteristics during cloud cavitation in this study.

Unsteady cavitation has been widely studied around hydrofoils and in internal flows [1, 5–7]. Experiments and simulations have shown that re-entrant jet and shock wave were the two main mechanisms leading to the occurrence of cloud cavitation [8–10]. Franc and Michel [11] reviewed studies of cavity closure and re-entrant jet during cloud cavitation. Kubota et al. [12] experimentally and numerically investigated unsteady cavitation on a hydrofoil. Numerous vortex structures including a large-scale vortex were observed with the cloud cavitation formation. Gopalan and Katz [13] used particle image velocimetry to record the cavitating flow structures and found that the cavitation significantly increased the vorticity and turbulence. Wosnik et al. [14] found five types of vortex structures accompanying the cloud cavitation in a NACA0015 hydrofoil wake in an LES

✉ Bin Ji
jibin@whu.edu.cn

¹ State Key Lab of Water Resources and Hydropower Engineering Science, School of Power and Mechanical Engineering, Wuhan University, Wuhan 430072, China

² Key Lab of Jet Theory and New Technology of Hubei Province, Wuhan University, Wuhan 430072, China

study. Cavitation–vortex interactions are an interesting and challenging topic that has been studied by many researchers [15, 16]. Budich et al. [17] simulated cavitating flows over a wedge and modeled the cavitating horseshoe and hairpin vortices. They demonstrated that vortex stretching and dilatation dominated the vorticity evolution. Dittakavi et al. [18] conducted an LES investigation of cavitating flow in a venturi nozzle. They found that the cavity collapse downstream of the venturi nozzle formed hairpin vortices and generated most of the vorticity. Long et al. [19] used LES to study cavitating flow in a jet pump with the vorticity transport equation to discuss the cavitation and vortex relationship and cavitation–vortex interactions. The literature shows that cloud cavitation generates numerous vortex structures and influences their evolution and how the cavity interacts with the vortex. However there appears to be few studies focusing on the abundant vortex structures and cavitation–vortex interactions in cloud cavitation behind spheres. In addition, other cavity shedding features may exist with the complex wake characteristics during the cloud cavitation behind a sphere, which still need to be further investigated.

Single phase flows around bluff bodies with vortex shedding in the wake have been studied with numerous experimental and numerical investigations [20–22]. However there have been few studies of cloud cavitation around a sphere. Brandner et al. [3] experimentally studied cavitating flows around a sphere at a constant Reynolds number with varying cavitation numbers. They analyzed the cavity inception, detachment and collapsing based on the recorded cavity shapes. They investigated the cavity shedding and spectral characteristics using wavelet analyses which showed two distinct peak regions for cavitation numbers between 0.6 and 0.9. De Graaf et al. [4] extended the experimental investigations of Brandner et al. [3] to describe the cloud cavitation evolution in detail for various cavitation numbers with the cavity shedding phenomena divided into three regimes based on three causes of shedding, i.e. Kelvin–Helmholtz instabilities and attached and detached re-entrant jets. However, these experimental studies have rarely investigated the cavitation–vortex interactions in the sphere wake due to the limited experimental data. Cheng et al. [23], Pendar and Roohi [24], and Kolahan et al. [25] all used numerical models to reproduce experimentally observed cavitating flows around a sphere, but their studies paid little attention to the cavitation evolution and vortex shedding in the wake. Hence, the current study presents an LES investigation of the cloud cavitation characteristics and the vortex structures in the sphere wake as an extension of previous studies.

The main objectives of this paper on cloud cavitation around a sphere are to (1) reproduce and investigate cavitating flows around a sphere over a wide range of cavitation numbers ($0.36 \leq \sigma \leq 0.9$), (2) investigate the effect of the mesh resolution and carry out LES verification and validation to

demonstrate the LES accuracy based on five refined meshes, (3) analyze three modes associated with the local cavitating flow structures in the sphere wake for $\sigma = 0.75$ (i.e. the periodic cavitation mode, high Strouhal number mode and low Strouhal number mode, which are distinguished based on the spectral characteristic of the velocity at ten evenly distributed monitoring points in the wake), (4) describe three cavity shedding regimes identified by the cavitation patterns and vortex structures in the sphere wake for $\sigma = 0.75$, (5) study the vortex structure evolution related to the cloud cavity and the Cavitation–vortex interaction in the sphere wake for $\sigma = 0.75$.

2 Governing equations

2.1 LES method

The incompressible Navier–Stokes equations were solved with a transport equation for the vapor volume fraction to model the liquid/vapor two-phase flow. LES was used with a filtering operation to the incompressible Navier–Stokes equations with the dynamic Smagorinsky model proposed by Germano et al. [26] and modified by Lilly [27] to model the subgrid stresses.

The filtered variable signed by an overbar is written as

$$\bar{\phi}(x) = \int_D \phi(x') G(x, x') dx', \quad (1)$$

where D and G indicate the domain and filter function respectively. The finite-volume discretization in this paper itself can implicitly carry out the filtering operation

$$\bar{\phi}(x) = \frac{1}{V} \int_v \phi(x') dx', \quad x' \in v, \quad (2)$$

where V is the volume of a computational cell. The filter function used here is

$$G(x, x') = \begin{cases} 1/V, & x' \in v, \\ 0, & x' \in \text{otherwise.} \end{cases} \quad (3)$$

Then the LES conservation equations for the mixture flow are

$$\frac{\partial \rho_m}{\partial t} + \frac{\partial(\rho_m \bar{u}_j)}{\partial x_j} = 0, \quad (4)$$

$$\frac{\partial(\rho_m \bar{u}_i)}{\partial t} + \frac{\partial(\rho_m \bar{u}_i \bar{u}_j)}{\partial x_j} = - \frac{\partial \bar{p}}{\partial x_i} + \frac{\partial}{\partial x_j} \left(\mu_m \frac{\partial \bar{u}_i}{\partial x_j} \right) - \frac{\partial \tau_{ij}}{\partial x_j}, \quad (5)$$

where τ_{ij} are the subgrid-scale (SGS) stresses and p_m , ρ_m and μ_m denote the mixture pressure, density and dynamic viscosity. ρ_m and μ_m are defined as

$$\rho_m = \rho_v \alpha_v + \rho_l (1 - \alpha_v), \quad (6)$$

$$\mu_m = \mu_v \alpha_v + \mu_l (1 - \alpha_v), \quad (7)$$

where subscripts l and v indicate the liquid and vapor phases and α_v is the vapor volume fraction for the cavitation process.

τ_{ij} are unknown and defined as

$$\tau_{ij} = \rho_m (\overline{u_i u_j} - \overline{u_i} \overline{u_j}). \quad (8)$$

The Boussinesq hypothesis is used to compute τ_{ij} by scaling the strain rate tensor, $\overline{S_{ij}}$, as

$$\tau_{ij} - \frac{1}{3} \tau_{kk} \delta_{ij} = -2 \mu_{sgs} \overline{S_{ij}}, \quad (9)$$

$$\overline{S_{ij}} = \frac{1}{2} \left(\frac{\partial \overline{u_i}}{\partial x_j} + \frac{\partial \overline{u_j}}{\partial x_i} \right), \quad (10)$$

where μ_{sgs} represents the SGS turbulent viscosity. The isotropic part of τ_{ij} , i.e. τ_{kk} is not modeled, but is added to the filtered static pressure. The SGS viscosity is modeled as

$$\mu_{sgs} = \rho_m L_s^2 |\overline{S}|, \quad (11)$$

$$L_s = \min(\kappa y_{wall}, C_s \Delta), \quad (12)$$

where C_s is the Smagorinsky constant, Δ is the filter width, κ is the von Kármán constant and y_{wall} is the distance to the closest wall. Germano et al. [26] and subsequently Lilly [27] proposed the dynamic Smagorinsky model to dynamically compute the Smagorinsky constant based on the information provided by the resolved scales of motion. At the test-filtered field level, the test-filtered SGS stress T_{ij} can be written as

$$T_{ij} = \overline{\widehat{\rho_m u_i u_j}} - \left(\overline{\widehat{\rho_m u_i}} \overline{\widehat{\rho_m u_j}} / \overline{\widehat{\rho_m}} \right). \quad (13)$$

T_{ij} and τ_{ij} are modeled as

$$T_{ij} = -2C \rho_m \widehat{\Delta}^2 |\widehat{S}| \left(\widehat{S}_{ij} - \frac{1}{3} \widehat{S}_{kk} \delta_{ij} \right), \quad (14)$$

$$\tau_{ij} = -2C \rho_m \Delta^2 |\overline{S}| \left(\overline{S}_{ij} - \frac{1}{3} \overline{S}_{kk} \delta_{ij} \right), \quad (15)$$

where $\widehat{\Delta} = 2\Delta$ and $C = C_s^2$. The grid filtered SGS and the test-filtered SGS are related as

$$L_{ij} = T_{ij} - \widehat{\tau}_{ij}. \quad (16)$$

Then the coefficient can be calculated as

$$C = \frac{(L_{ij} - L_{kk} \delta_{ij} / 3) M_{ij}}{M_{ij} M_{ij}}, \quad (17)$$

$$M_{ij} = -2 \left(\rho_m \widehat{\Delta}^2 |\widehat{S}| \widehat{S}_{ij} - \rho_m \Delta^2 |\overline{S}| \overline{S}_{ij} \right), \quad (18)$$

$$C_s = \sqrt{C}. \quad (19)$$

2.2 Cavitation model

The aforementioned system need to be closed by a vapor transport equation

$$\frac{\partial(\rho_v \alpha_v)}{\partial t} + \frac{\partial(\rho_v \alpha_v u_i)}{\partial x_i} = m_e - m_c, \quad (20)$$

where m_e and m_c on the right side denote the cavitation mass transfer. The generalized Rayleigh–Plesset equation is usually used to calculate these mass transfer rates and is written for bubble dynamics as

$$R_B \frac{d^2 R_B}{dt^2} + \frac{3}{2} \left(\frac{dR_B}{dt} \right)^2 = \frac{p_v - p}{\rho_l} - \frac{4\nu_l}{R_B} \frac{dR_B}{dt} - \frac{2S}{\rho_l R_B}, \quad (21)$$

where R_B represents the bubble radius, p_v is the saturated vapor pressure, p is the local far-field pressure and S is the surface tension force. Neglecting the second-order terms, the viscous effect and the surface tension force gives

$$\frac{dR_B}{dt} = \sqrt{\frac{2}{3} \frac{|p_v - p|}{\rho_l}}. \quad (22)$$

Zwart et al. [28] proposed a total interphase mass transfer per unit volume to account for the evaporation and condensation. For N_B bubbles per unit volume, α_v can be calculate as

$$\alpha_v = \frac{4}{3} \pi R_B^3 N_B. \quad (23)$$

The total interphase mass transfer rate for N_B bubbles per unit volume is

$$m = N_B \rho_v \frac{dV_B}{dt} = \frac{3\alpha_v \rho_v}{R_B} \frac{dR_B}{dt}, \quad (24)$$

where V_B represents the bubble volume.

The mass transfer equations to close Eq. (20) are then

$$m_e = F_{vap} \frac{3\alpha_{nuc}(1 - \alpha_v)\rho_v}{R_B} \sqrt{\frac{2}{3} \frac{\max(p_v - p, 0)}{\rho_l}}, \quad (25)$$

$$m_c = F_{cond} \frac{3\alpha_v \rho_v}{R_B} \sqrt{\frac{2}{3} \frac{\max(p - p_v, 0)}{\rho_l}}, \quad (26)$$

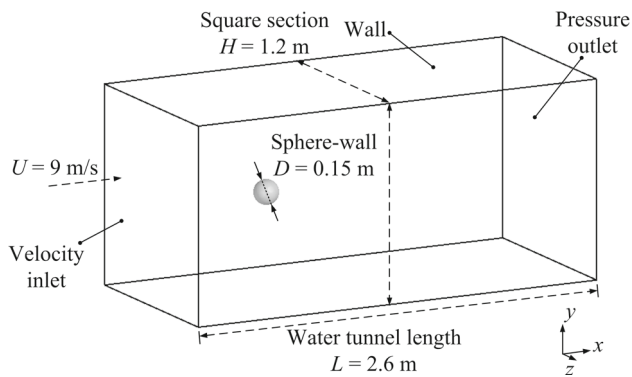


Fig. 1 Computational domain and boundary setup

where α_{nuc} denotes the volume fraction of nucleation sites and F_{vap} and F_{cond} are empirical constants for vaporization and condensation. The constants used in the Zwart–Gerber–Belamri cavitation model [28] are $R_B = 10^{-6}$ m, $\alpha_{nuc} = 5 \times 10^{-4}$, $F_{vap} = 50$, $F_{cond} = 0.01$. These setup in this model have been extensively validated with good agreement with experiments in simulating complex cavitating flows [16, 29, 30].

3 Numerical setup

Figure 1 shows a sketch of the sphere body, computational domain and boundary setup. A uniform velocity ($U = 9$ m/s) was imposed on the velocity inlet boundary. The sphere surface with a no-slip wall setup was placed at the center of the computational domain with a diameter, D , of 0.15 m. The Reynolds number was constant at $Re = 1.5 \times 10^6$. A fixed static pressure, p_{out} , at the outlet boundary was derived from the cavitation number σ . Re and σ were defined as

$$Re = \frac{UD}{\nu_l}, \quad (27)$$

$$\sigma = \frac{p_{out} - p_v}{0.5\rho_l U^2}. \quad (28)$$

The simulations used seven cavitation numbers (i.e. $\sigma = 0.36, 0.4, 0.5, 0.6, 0.75, 0.8$ and 0.9). The fluid properties used in this study were $\rho_l = 1000$ kg/m³, $\rho_v = 0.02308$ kg/m³, $\mu_l = 9 \times 10^{-4}$ kg/(m·s), $\mu_v = 1 \times 10^{-5}$ kg/(m·s) and $p_v = 2300$ Pa. The sphere geometry, simulated cavitation conditions and fluid properties were all based on the experiments of Brandner et al. [3] and De Graaf et al. [4], which were also adopted by Cheng et al. [23], Pendar and Roohi [24], and Kolahan et al. [25] in the sphere cavitation simulations.

Table 1 shows the mesh numbers and time-step setup for the five refined structured meshes using the same topology.

Table 1 Mesh information and setup for the sphere cavitation simulations

Mesh	Number of elements	Time-step (s ⁻¹)
1	16,919,464	4×10^{-5}
2	9,793,905	4.8×10^{-5}
3	5,655,922	5.76×10^{-5}
4	3,250,527	6.912×10^{-5}
5	1,876,553	8.2944×10^{-5}

These five meshes were refined with a constant ratio r ($r = 1.2$) along the three coordinate axes. The time-step changes used the same ratio ($r = 1.2$) with the mesh that gave the same Courant number in the calculation. A sketch of structured mesh around the sphere is shown in Fig. 2. The y^+ was about 1 on the sphere surface, and the first mesh spacing to the wall was the same for all the meshes to prevent the change of first mesh spacing influencing the calculation of SGS viscosity and application of LES verification and validation.

The bounded central differencing scheme was used for the spatial discretization of the momentum equations. The bounded second order implicit scheme was used for the transient terms. The pressure–velocity coupling used the SIMPLEC algorithm. The transient cavitating flow simulations were initialized using a convergent result with no cavitation reached with a convergence criterion of 10^{-6} root mean square (RMS) residual. The internal iteration steps for the unsteady cavitating flow in each time-step are within 40 with a convergence criterion of 10^{-4} RMS residual. The total numerical flow time exceeded 0.9 s for all the meshes. All the calculations were performed on the supercomputing system with 2 threads and 32 processors (Intel Xeon E5-2630 v3 \times 86_64, 2.4 GHz), and the transient calculation with the largest mesh, Mesh 1, requires over 1 month.

4 Results and discussion

4.1 Comparison of the experiments and simulations using the five refined meshes

Figure 3 shows four transient cavitation patterns selected for different flow states as described in the experimental study by De Graaf et al. [4] for $\sigma = 0.75$. In Fig. 3a, the re-entrant jet forms as the cavity grows and only influences the cavity tail. Most of the liquid–vapor surface is not disturbed by the re-entrant flow. The re-entrant flow shown in Fig. 3b has reached to the sphere surface and the liquid–vapor surface becomes wavy. However, the main body of the cavity is still attached to the sphere. Several sections of

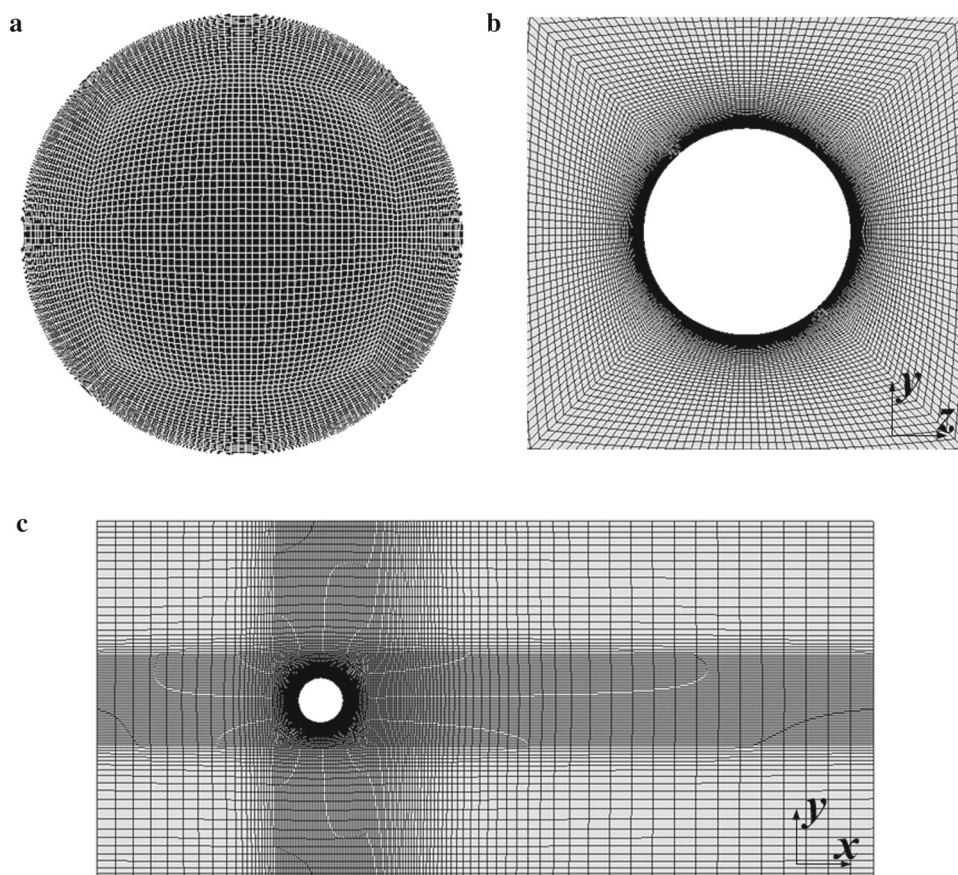


Fig. 2 Structured mesh around the sphere for Mesh 5. **a** Mesh distribution on the sphere surface, **b** mesh distribution around the sphere, and **c** side view on the x - y plane

the sphere can be seen in Fig. 3c and the stable cavity surface upstream breaks down into strips of cavitating vortex filaments due to the re-entrant flow moving upstream. The cavitating vortex filaments in the circumferential direction finally disappear or move downstream. The attached cavity in Fig. 3d is totally cut off by the re-entrant jet and the cavity leading edge disappears completely. The cloud cavitation forms with numerous small-scale cavitating vortex filaments and complex vortex structures. Some of the cavity leading edge can still be seen around the circumference. In addition, the oblique shedding cavity and a new growing cavity exist simultaneously in different regions around the sphere.

All five meshes successfully model the cavity growing and shedding, and the detailed cavitation structures (the fine small-scale cavitating vortex filaments and the vortex cavitation) are captured more clearly with meshes finer than Mesh 3. The vortex cavitation in the wake due to the low pressure in the vortex tube becomes more apparent with the better mesh resolution, and Mesh 1 captures the most detailed cavitating vortex structures. The mesh size has little effect on the mean

cavity length and shape as shown in Fig. 3e with only a few differences observed at the cavity tail.

4.2 Comparison with experiments at various cavitation numbers

Figure 4 compares the experimental [3, 4] and predicted cavitation patterns around the sphere for various cavitation numbers. As discussed in the previous section, the cavitation patterns and structures are well reproduced with mesh resolutions finer than Mesh 3, so the predicted cavitation patterns in Fig. 4 were presented using Mesh 3 as an example. The simulations are compared with the experimental results for (1) the supercavitation regime when $\sigma < 0.4$ and (2) the cloud cavitation regime when $0.4 < \sigma < 0.9$. In these two cavitation regimes, the cavity shape and cavity length around the sphere are reasonably reproduced by the current simulations. The cavitation leading edge location seems to be a little overestimated in Fig. 4, but it has little influence on the main characteristics of sheet cavitation and cloud cavitation at the sphere wake. This phenomenon is also observed in sphere cavitation simulations by Cheng et al. [23], Pendar

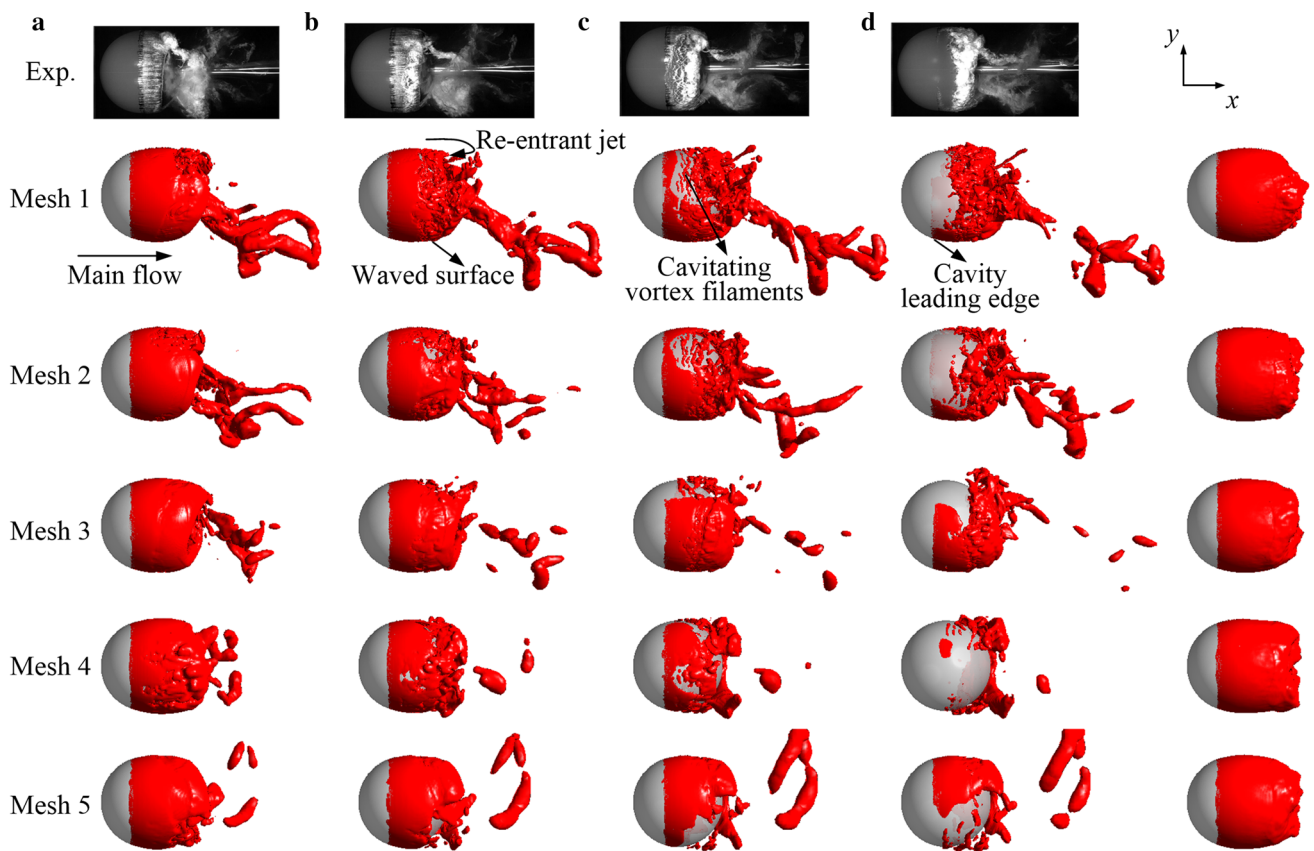


Fig. 3 Experimental cavitation patterns [4] and simulation results using five meshes. The numerical results in **a–d** denote the instantaneous cavitation patterns given by an isosurface of $\alpha_v = 0.1$. Last column: time-averaged cavitation patterns given by an isosurface of $\alpha_v = 0.1$. $\sigma = 0.75$, $Re = 1.5 \times 10^6$

and Roohi [24], and Kolahan et al. [25]. The reason of overestimation might be that cavitation inception in simulation occurs once the pressure is lower than the vapor pressure, while in real world it is influenced by cavitation nuclei and pressure [11].

Figure 5 displays the distributions of the cavitation, local pressures and streamwise velocities in the wake for $\sigma = 0.36$ and $\sigma = 0.6$ as examples to clarify the difference between the supercavitation and cloud cavitation regime regimes. In the supercavitation regime ($\sigma = 0.36$), the overall cavity shape remains almost unchanged. In the near wake shown in Fig. 5a, the liquid–vapor interface is very clear. Further downstream, the liquid–vapor interface starts to diffuse into a larger region and becomes somewhat wavy with the separated shear layer becoming unstable, which indicates the transition to turbulent flow in the adjacent shear layer. This phenomenon was observed by Brandner et al. [3] in their experiments. A few cavitation vortex filaments can be seen sporadically near the supercavitation tail in Fig. 4. The cavity tail seems to be a little unstable due to the influence of the re-entrant flow as visualized in Fig. 5a. The re-entrant flow begins at the supercavitation tail due to the local high pressure and grows upstream a relatively short distance. At this cavitation num-

ber, the cavity becomes sufficiently long so that the re-entrant jet no longer cuts off the cavity.

In the cloud cavitation regime ($0.4 < \sigma < 0.9$), the pictures in Fig. 4 show that the cavity surface becomes unstable due to the influence of the re-entrant jet. The moderate cavity length at intermediate σ enables nearly fully development of the re-entrant jet, which leads to the cutoff of the sheet cavity and then total extinction of the cavity leading edge. As the cavitation number increases to much higher values ($\sigma = 0.9$), the sheet cavitation sheds from the sphere surface with a ring shaped cavity with many small-scale bubble cloud structures in the near wake. The cavity, local pressure and velocity contours for $\sigma = 0.6$ in Fig. 5 clearly show the re-entrant jet, which moves upstream to the sphere surface due to the strong adverse pressure gradient. Two local high pressure regions are seen in Fig. 5b at the upper and lower surfaces of the sphere. At the upper surface of the sphere, the cavity is cut off by the re-entrant jet and the shedding cloud cavitation is conveyed downstream. At the lower surface of sphere, an attached sheet cavity grows and its tail is lifted up by the head of the forming re-entrant jet. Oblique cavity shedding, one significant feature observed in the experiments (Brandner et al. [3] and De Graaf et al. [4]), was successfully

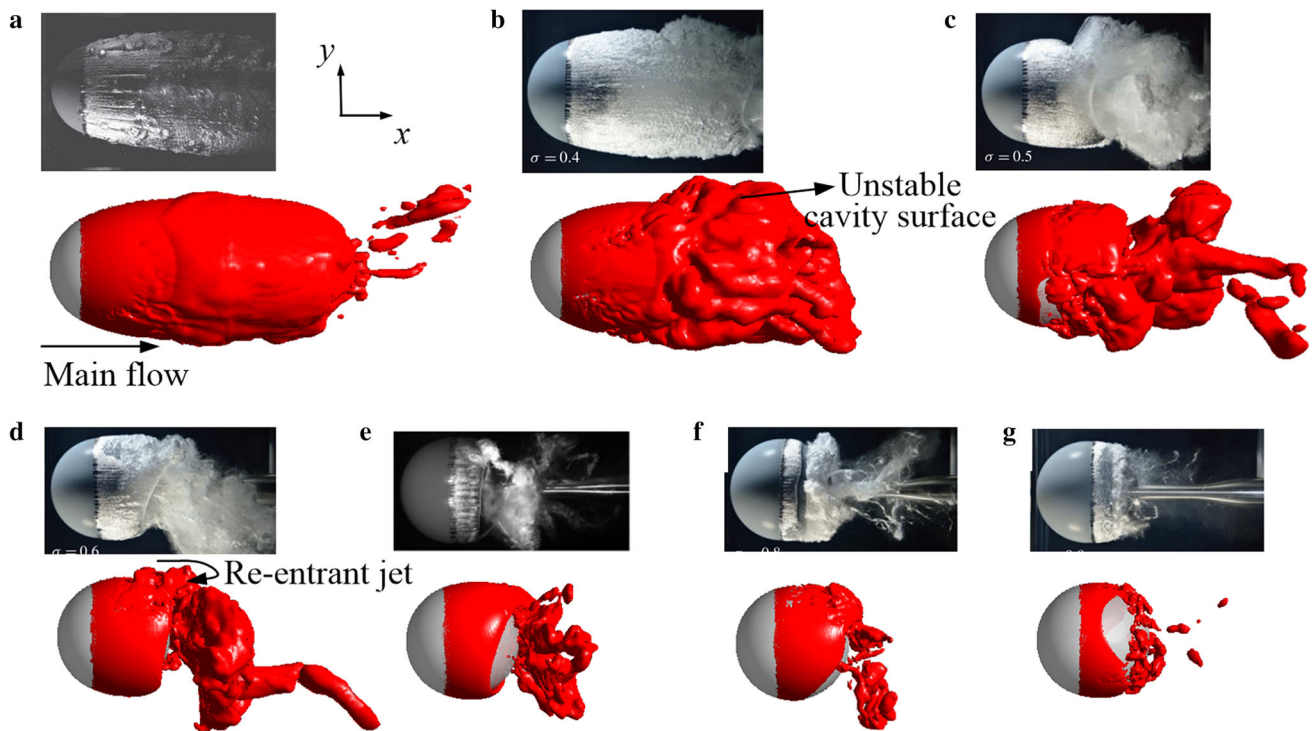


Fig. 4 Experimental and simulated cavitation patterns at various cavitation numbers, **a** $\sigma = 0.36$, **b** $\sigma = 0.4$, **c** $\sigma = 0.5$, **d** $\sigma = 0.6$, **e** $\sigma = 0.75$, **f** $\sigma = 0.8$, and **g** $\sigma = 0.9$. The experimental results [3, 4] are shown in the first line for each cavitation number with the predicted cavity patterns shown by isosurface $\alpha_v = 0.1$ in the second line. $Re = 1.5 \times 10^6$

reproduced in the current simulations. At intermediate σ in the cloud cavitation regime, the oblique cavity shedding is usually accompanied by large-scale vortex structure, as will be discussed in the following sections.

Figure 6 shows the local velocity distributions again to illustrate the change in the separated shear layer for the two cavitation numbers. As shown in Fig. 6a, the separated shear layer is clearly seen downstream of the sphere as was observed by Brandner et al. [3]. At about mid-length along the cavity surface, the cavity surface become wavy as the separated shear layer becomes unstable and changes into a turbulent shear layer due to Kelvin–Helmholtz instabilities. Figure 6 shows that the separated shear layer is disturbed and becomes unstable much earlier just above the surface as the re-entrant jet moves towards the cavity leading edge, which may indicate that the re-entrant jet accelerates the transition to turbulence in the stable shear layer.

4.3 Comparison of the spectral data of cavity shedding and lift coefficient

Few experimental quantitative data, e.g. spectral data of cavitation evolution, are available in the available experimental studies [3, 4], while we are still trying to do more quantitative comparison of the spectral data with the limited experiments. Table 2 shows the comparison of the dominant frequencies

for four cavitation numbers based on the available experimental data and our simulation results with Mesh 3. There are two main peak frequencies of cavitation evolution when $\sigma = 0.9, 0.8$ and 0.6 , which the higher and lower frequencies might be resulted by the periodic cavitation evolution and interaction between sheet and cloud cavitation respectively. When $\sigma = 0.4$, the cavity length becomes long enough and interaction between sheet and cloud cavitation is not significant, so there is only one dominant frequency. In order to further demonstrate the accuracy of our numerical results, we also present the comparison of the dominant frequencies of lift coefficient between the numerical results by Cheng et al. [23] and in this paper for $\sigma = 0.75$, as shown in Table 3. The results in Tables 2 and 3 demonstrate that current simulation results have shown well agreement with these data and good calculation accuracy is achieved.

4.4 LES error analysis using the verification and validation method

Numerical results are often compared with experimental data to demonstrate the simulation accuracy, such as the comparisons of the cavitation patterns here. However, they still seem to be limited to argue the simulation reliability due to the lack of quantitative accuracy data (e.g. simulation errors or uncertainties as in experimental uncertainties). The verifica-

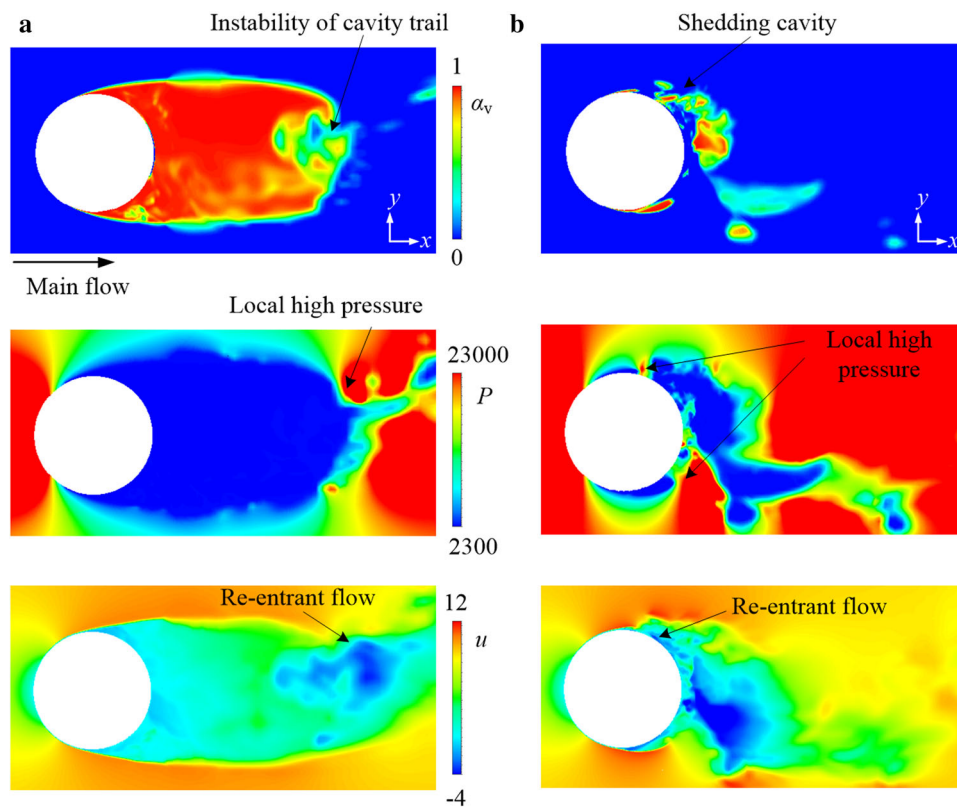


Fig. 5 Cavity shape, local pressure and velocity distributions for **a** $\sigma = 0.36$ and **b** $\sigma = 0.6$. First line: vapor volume fractions, second line: pressures, third line: streamwise velocity, u (i.e. velocity component in the x -axis). $Re = 1.5 \times 10^6$

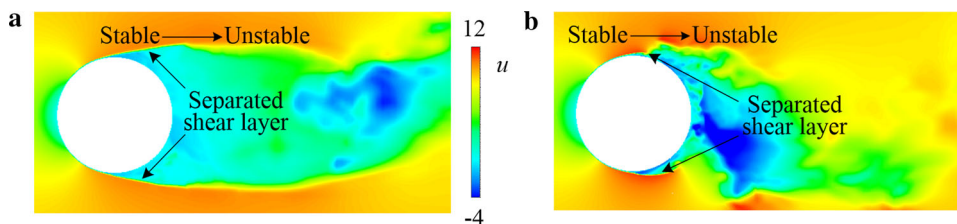


Fig. 6 Local streamwise velocity distributions for **a** $\sigma = 0.36$ and **b** $\sigma = 0.6$. $Re = 1.5 \times 10^6$

Table 2 Comparison of the dominant frequencies of cavitation evolution

σ	Experiments [3, 4]		Simulations	
	f_1 (Hz)	f_2 (Hz)	f_1 (Hz)	f_2 (Hz)
0.9	12	43.2	10.27	41.09
0.8	14.4	24	11.14	25.62
0.6	6.6	21	7.52	22.56
0.4	6	–	7.12	–

tion and validation (V&V) method has been used in many studies to evaluate the accuracies of physical models and numerical results with quantitative data [31]. The LES errors are evaluated here using V&V method to demonstrate the simulation accuracy [16].

Table 3 Comparison of the dominant frequencies of lift coefficient for $\sigma = 0.75$

Mesh	f_1 (Hz)	f_2 (Hz)
Cheng et al. [23]	11	34.91
Mesh 1	11.52	33.13
Mesh 2	11.47	34.41
Mesh 3	11.54	34.62
Mesh 4	10.72	32.15
Mesh 5	10.57	32.76

The total error between the LES result and a numerical benchmark for Mesh 1 can be estimated as

$$S_1 - S_C = c_N (h^*)^{PN} + c_M \Delta^{PM}, \tag{29}$$

where S_1 is variable solution, S_C is the numerical benchmark, and Δ is the filter width. The numerical benchmark denotes the exact numerical solution approximately, while it is usually not able to directly obtain in practical application. So the numerical benchmark in practical calculations can be sometimes replaced by high accuracy numerical results. Two terms on the right side of Eq. (29), $c_N(h^*)^{p_N}$ and $c_M\Delta^{p_M}$, are the numerical error and the modeling error. c_N and c_M are coefficients and p_N and p_M are the orders of accuracy for the numerical and modeling errors. $h^* = \sqrt{h\Delta t}$, where h is the mesh size and Δt is the time step. h is computed according to the volume of the computational cell V , i.e. $h = V^{1/3}$.

As with the five-equation and simplified three-equation methods used to study hydrofoil cavitation [16], the LES numerical and modeling errors can be estimated based on the results for the five refined meshes shown in Table 1. Similar to Eq. (29), five equations constructed by five refined meshes shown in Table 1 can be used to obtain all unknown coefficients in Eq. (29). With the help of optimization toolbox in MATLAB, the highly non-linear five equations can be solved robustly. To simplify the calculation of LES errors in the practical application, the values of p_N and p_M , which are solved from five equations based on a representative variable, can be set as constant to calculate the LES errors for other different variables. Finally due to the values of p_N and p_M are constant, we can calculate the LES numerical error and modeling error with simplified linearized three equations. Usually mesh triplet 1-3-5 is recommended to calculate the LES errors for Mesh 1.

The calculated LES total relative error for the time-averaged total cavity volume for Mesh 1 is 2.6388×10^{-4} , which is small and indicates the good accuracy of the predicted cavity volume. Ten monitoring points were arranged in sphere wake as shown in Fig. 7 to record the velocity to calculate the LES errors for the time-averaged streamwise velocity, u . These ten points are labeled as u_1 – u_{10} and are evenly distributed behind the sphere with an increment of $0.2D$. These monitoring points shown in Fig. 7 are the representative locations at the sphere wake within $2D$ long. This range at the sphere wake within $2D$ long contains most of the turbulent cavitating flow characteristics, such as the transient cavitation evolution and vortex structures which will be discussed below. The absolute values of the LES numerical and modeling errors are presented in Fig. 8 for the time-averaged streamwise velocity at the ten monitoring points. The LES errors gradually decrease from u_1 to u_3 as the cavitation influence gradually decreases in the wake at monitoring points further from the sphere. The errors then increase at u_4 due to the complex interactions between the shedding cavity and the newly formed sheet cavity, as will be discussed below. The LES errors then decrease sharply from u_4 to u_6 because of the rapid decrease of the influence of the unstable cavity and the complex interactions. The errors remain small from

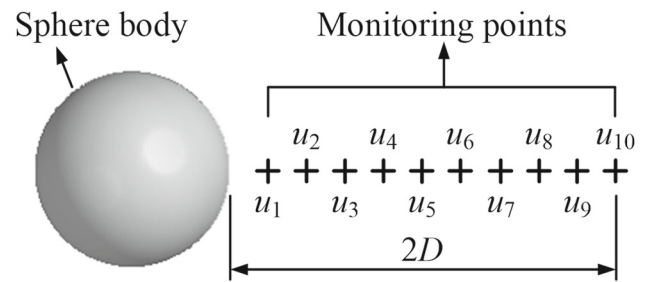


Fig. 7 Locations of the ten monitoring points

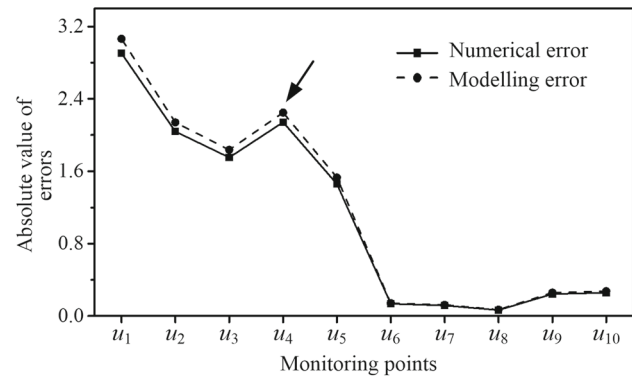


Fig. 8 Absolute values of the LES errors for the time-averaged streamwise velocity. $\sigma = 0.75$, $Re = 1.5 \times 10^6$

u_6 to u_{10} with a slight increase at u_9 and u_{10} , which may be resulted by the reduced mesh resolution in the far wake (e.g. u_9 and u_{10}).

4.5 Spectral characteristics of the sphere wake

The wake characteristics of the sphere cavitating flow were further analyzed using a spectral analysis of the wake. The results for $\sigma = 0.75$ for Mesh 1 were chosen as an example to further study the complex cavitating flow structures in this section and the cavitation–vortex interactions in the next section.

The dominant frequencies distributions for the velocity u at the ten monitoring points shown in Fig. 7 are presented in Fig. 9. The power spectral density is plotted in terms of the Strouhal number, $St = fD/U$, where f is the frequency obtained from a fast Fourier transform for the transient velocity u signal for more than 15 cavity cycles. The dominant frequencies show three main modes with Mode 1 as the periodic cavitation mode, Mode 2 as the high Strouhal number mode and Mode 3 as the low Strouhal number mode. The low and high modes (not exactly the same as the low and high Strouhal number modes in this study) were also mentioned by Brandner et al. [32] and Venning et al. [33] for cavitating flows behind spheres. The high Strouhal number mode here is not the same as the classical “high” mode seen in single phase flows around spheres which is due to the Kelvin–Helmholtz

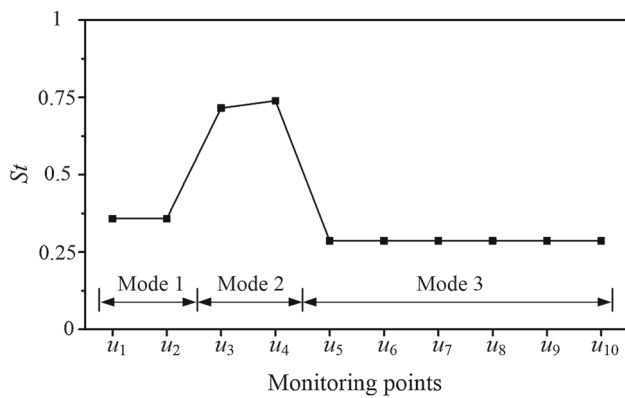


Fig. 9 Dominant frequencies for the velocity u at the ten monitoring points. $\sigma = 0.75$, $Re = 1.5 \times 10^6$

instability in the separated shear layer [20, 34]. The periodic cavitation mode includes points u_1 and u_2 and its dominant Strouhal number is 0.358. The low frequency mode includes points u_5 – u_{10} , and its dominant Strouhal number is 0.286. The peak frequency may be related to the flow structures in the local region, so this is discussed more when discussing the classifications of the three modes in the wake.

4.5.1 Mode 1: periodic cavitation mode

Figure 10 shows the power spectral density for the predicted total cavity volume, V_c , with the peak frequency marked by the red arrow as 0.358. This peak St is equal to values at points u_1 and u_2 as shown in Fig. 9, which indicates that the most significant effect in this region is the periodic cavity evolution. Figure 11 shows the vapor volume variations with time and details of three typical cycles (i.e. cycle A, cycle B and cycle C) that show the detailed flow structures around the sphere below. Figure 11 also shows that the cavity evolution around the sphere is a quasi-periodic process with growing and contracting cavities, as also shown in Fig. 12a. The dominant frequency mainly indicates the effect of the periodic cavity growing and contracting with u_1 and u_2 located in the regions most influenced by the periodic cavity growth and collapse.

4.5.2 Mode 2: high Strouhal number mode

Brandner et al. [3] found two peak St for cavitation numbers changing from 0.5 to 0.8 whose magnitudes corresponded with the two peaks in Mode 2 and Mode 3 in this study. They pointed out that there was only one dominant frequency (the lower value) after the interactions between the shedding cloud cavitation and the new growing sheet cavitation disappeared. In this study, the high frequency spectral features also seem to depend on the complex flow structures resulting

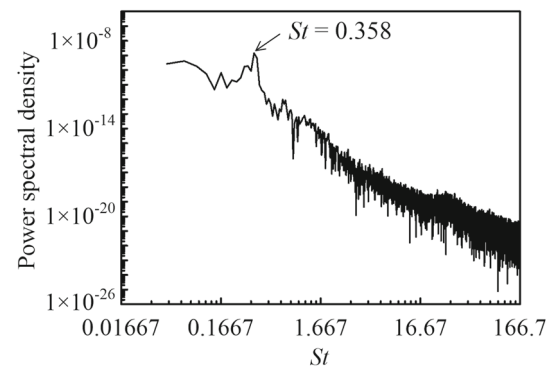


Fig. 10 Power spectral density for the total cavity volume, V_c . $\sigma = 0.75$, $Re = 1.5 \times 10^6$

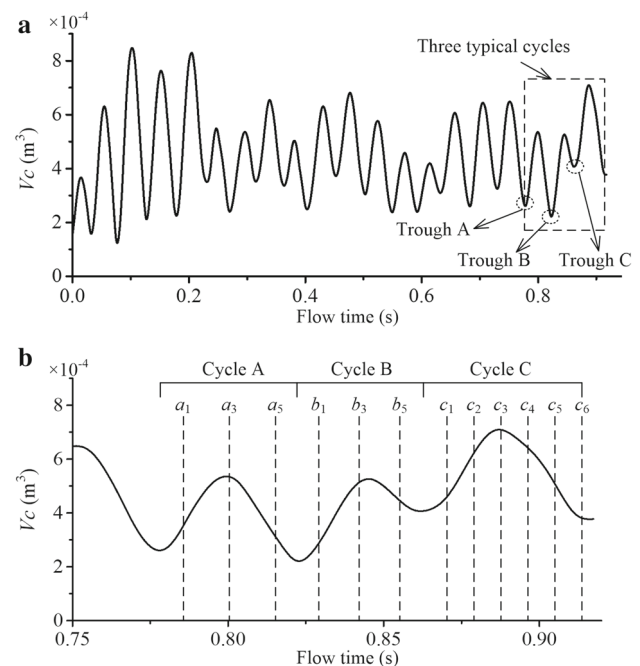


Fig. 11 Simulated total cavity volumes for **a** the entire simulation process and **b** three typical cycles. $\sigma = 0.75$, $Re = 1.5 \times 10^6$

due to the interactions between the shedding cloud cavitation and the new growing sheet cavitation.

In this mode, the peak St for u_3 and u_4 are higher than for the other points. As shown in Fig. 12a for cycle C, the shedding cloud cavity still connects with the newly formed sheet cavity instead of being totally cutoff and losing its connection with the new sheet cavity as is usually seen in cloud cavitation in hydrofoil [16]. The shedding cloud cavitation rotates along the flow direction, while the trailing edge of the sheet cavitation rotates along the circumferential direction. They meet in the near wake region. The cloud cavitation sheds at an oblique angle instead on the sphere surface all around the circumference. The oblique cavity shedding and the new sheet cavity grow alternate and can interact with each other in the wake.

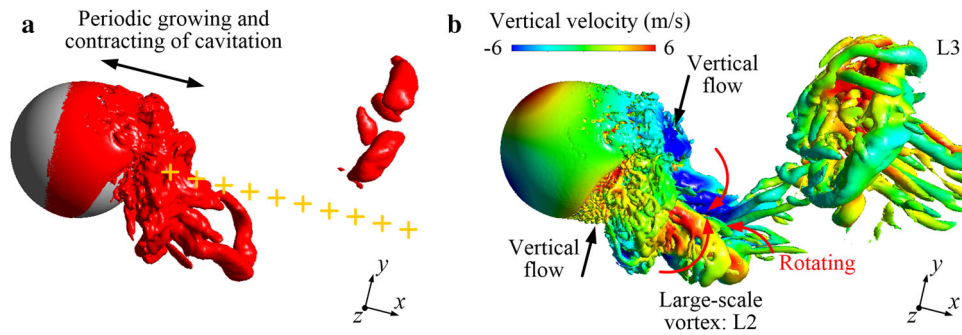


Fig. 12 Local flow structures in the wake at a typical moment ($T_0/4$ in cycle C). **a** Cavity patterns given by $\alpha_v = 0.1$ and **b** vortical structures given by $Q = 20,000 \text{ s}^{-2}$, $\sigma = 0.75$, $Re = 1.5 \times 10^6$

The vortical structures better illustrate the complex interactions between the shedding cloud cavity and the newly formed sheet cavity as shown in Fig. 12b and by the six transient vortex and cavitation structures in cycle C in Fig. 13. The vortical structures are shown by the isosurface of the Q -criterion calculated as $\frac{1}{2}(|\boldsymbol{\Omega}|^2 - |\mathbf{S}|^2)$ where $\boldsymbol{\Omega}$ is the vorticity tensor and \mathbf{S} is the strain tensor. As shown in Fig. 13a for cycle C, the oldest horseshoe vortex structure, L3, in cycle C has already existed for a while with its bottom still connected with the newly growing vortex structure L2. This connection weakens and finally breaks in Fig. 13c. The head of L2 convects downstream with many small-scale vortical structures forming behind the two legs of L2 while the tails of the two legs still tightly connected with the vortex sheet along the upper sphere surface. The complex interacting flow structures significantly influence the wake and may be the dominant effect for the u_3 and u_4 regions in this study.

4.5.3 Mode 3: low Strouhal number mode

The dominant frequencies from u_5 to u_{10} have the same peak St that is relatively low compared to those at monitoring points u_1 – u_4 . This is mainly influenced by the evolution of the large-scale vortex structure in the wake. Figure 13 shows three coherent vortex structures marked by blue dashed lines L1, L2 and L3. L3 is the oldest vortex structure shown in Fig. 13. Newly growing large-scale vortex structure L2, characterized by a horseshoe shape, is very clear (complete arched shape with two legs connected to one head) with the bold blue color indicating the downward movement of the vortex. Figure 12 shows the rotations of the two legs and the head in this horseshoe vortex. The vortex cavitation is also clearly seen due to the low pressure in the vortex tube of L2. Figure 12 also shows another vertical flow below the sphere that is growing and strengthening until it finally cuts off vortex structure L2. A new vortical structure, L1, forms at the end of this cycle as shown in Fig. 13e, f, but L1 consist of many smaller and finer vortical structures compared to L2. The cavitation patterns in Fig. 13e, f also show that the sheet cavity along the sphere

surface sheds with many bubbles with the formation of something like a vortex ring around the circumference. Unlike the horseshoe vortex cavitation that forms in the L2 vortex tube, no clear vortex cavitation forms in L1 which indicates that L1 is much weaker than L2.

The strong large-scale horseshoe vortex is transported far downstream with large energy fluctuations that significantly influence the far wake. However, this large-scale vortex structure does not seem to occur in each cavity cycle (this will be further discussed and verified at following section), which corresponds to a lower peak St compared to that for the periodic cavitation mode. The dominant frequency is relatively low for the six points (u_5 – u_{10}) in the far wake as was also observed in the experiments by Brandner et al. [3, 32].

In total, the periodic cavitation mode is resulted by the periodic cavity growth and collapse near the sphere wake, the high frequency mode is influenced by the interactions between the shedding cloud cavitation and the new growing sheet cavitation, and the high Strouhal number mode is due to the strong large-scale horseshoe vortex at the far sphere wake. All three of them are closely related to the cavitation evolution at the sphere wake.

4.6 Cavitation–vortex interactions in the sphere wake

4.6.1 Evolution of the cavitation and vortex structures

As shown in Fig. 11, the periodic cavity growth and contraction processes are similar in all the simulated cavity cycles. However, large differences in the detailed cavity shedding regimes are observed in the selected cycles (cycle A, cycle B and cycle C) in Figs. 14, 15, 16. Figure 11 shows the positions of the three cycles with three typical snapshots of the cavitation and vortical structures for each cycle presented in Figs. 14, 15, 16 (Fig. 14: cycle A with time points a_1 , a_3 and a_5 ; Fig. 15: cycle B with time points b_1 , b_3 and b_5 ; Fig. 16: cycle C with time points c_1 , c_3 and c_5).

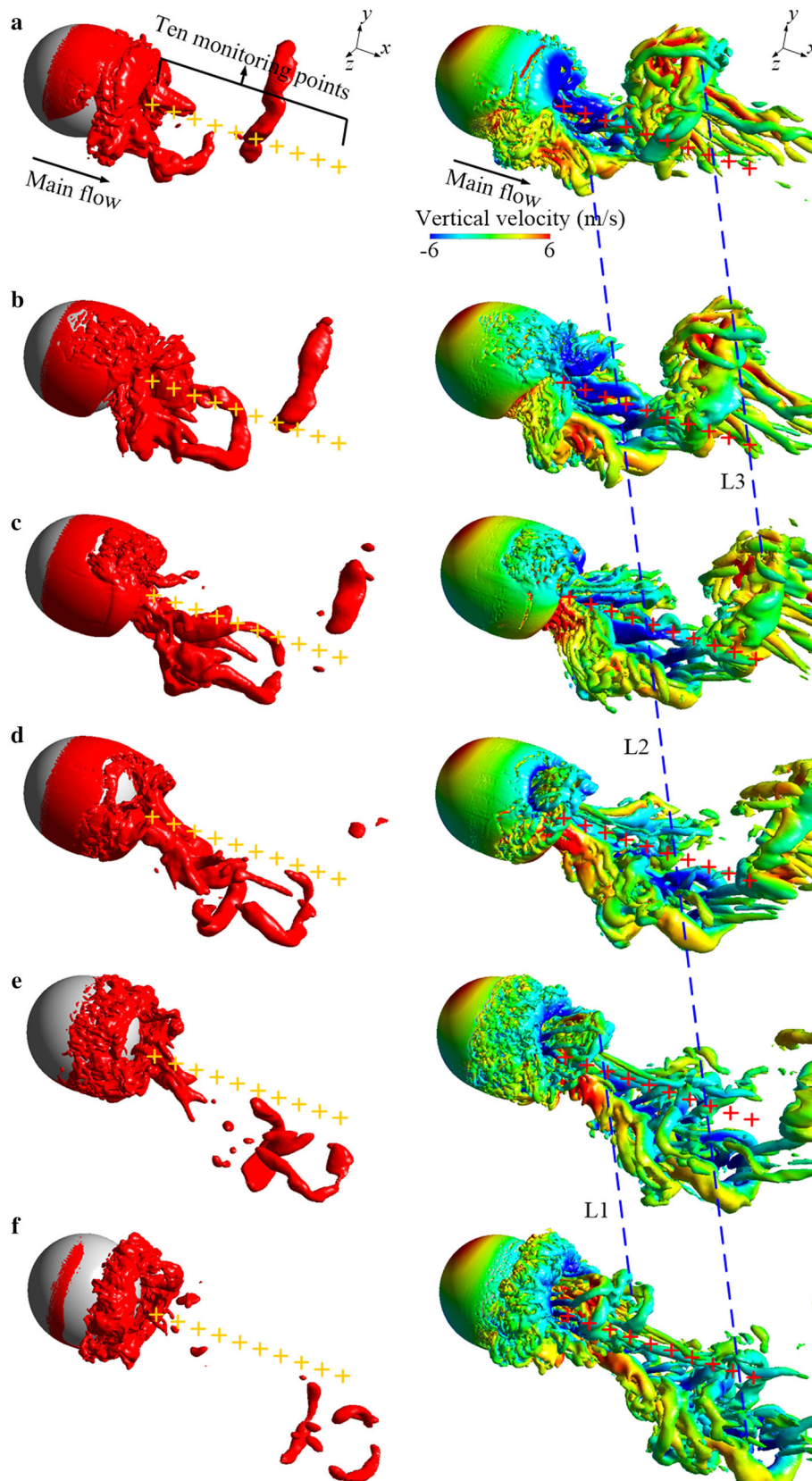


Fig. 13 Cavitation and vortical structures in cycle C, **a** $T_0/6$, **b** $2T_0/6$, **c** $3T_0/6$, **d** $4T_0/6$, **e** $5T_0/6$, and **f** $6T_0/6$ (left: cavity patterns given by isosurface $\alpha_v=0.1$; right: vortical structures given by isosurface $Q=20,000\text{ s}^{-2}$). Blue dotted lines denote three vortical structures generated in sequence (L1, L2 and L3). $\sigma=0.75$, $Re=1.5\times 10^6$

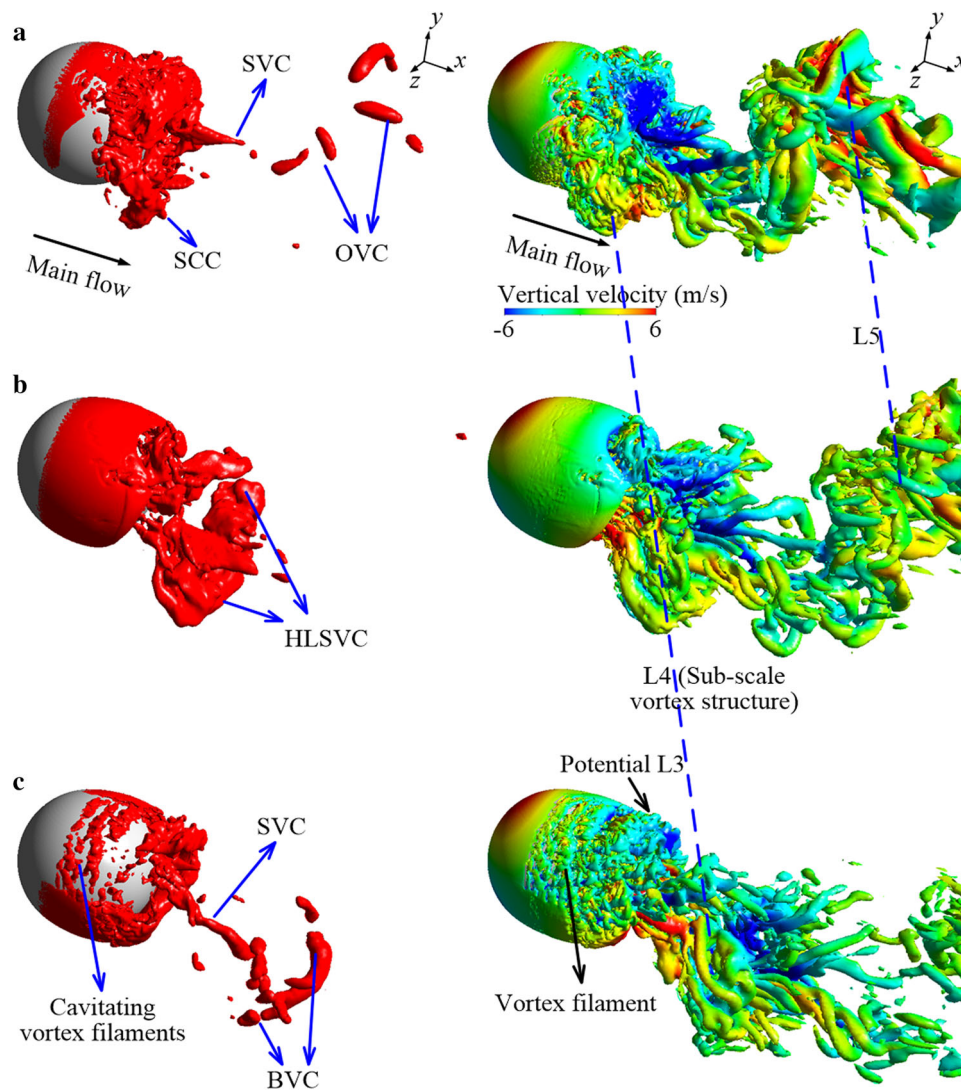


Fig. 14 Evolution of the transient cavitation and vortical structures in cycle A, **a** $T_0/6$, **b** $3T_0/6$, **c** $5T_0/6$ (left: cavity patterns given by isosurface $\alpha_v = 0.1$; right: vortical structures given by isosurface $Q = 20,000 \text{ s}^{-2}$). $\sigma = 0.75$, $Re = 1.5 \times 10^6$

The flows in cycles A and B shown in Figs. 14 and 15 start from troughs A and B marked in Fig. 11a which are the local minimums for moderate and low St within the three selected cycles. Figure 14 shows a nearly completed shedding cloud cavitation (SCC) on the lower sphere surface and a stream-wise vortex cavitation (SVC) behind the sphere. This SCC is connected to the newly growing sheet cavitation on the upper surface in a complex way, which is similar to the observation of Brandner et al. [3]. In Fig. 14b, the sheet cavitation continues to grow and the SCC develops into a horseshoe-like shaped vortex cavitation (HLSVC) that does not have clear, complete legs and head, so it is not the same as the horseshoe shaped vortex cavitation (HSVC) shown in Fig. 16a. So, this is labeled as HLSVC to distinguish from HSVC in this study. Vortex L4 consisting of many sub-scale vortices in Fig. 14b is also not the same as the large-scale vortex shown in Fig. 16b

which has a clearly dominant large-scale horseshoe shape. In Fig. 14c, the sheet cavitation that started growing in Fig. 14a breaks down into many cavitating vortex filaments along the upper sphere surface. Vortex structure L3 (labeled potential L3 in Fig. 14c) is going to form as in Fig. 15a. The wake in Fig. 14c has only a few SVC and a broken vortex cavitation (BVC) that developed from the HLSVC.

In Fig. 15a, the cavitating vortex filaments mentioned in Fig. 14c have disappeared or been convected into the SCC with a new sheet cavitation formed on the lower surface. The BVC develops into an odd vortex cavitation (OVC) in the far wake. Vortex structure L3 also occurs in this cycle with many small-scale vortices instead of large-scale or sub-scale vortices. So L3 is labeled as a fine vortex structure in this study as shown in Fig. 15b. In addition, no clear HSVC or HLSVC form in Fig. 15 with only some bro-

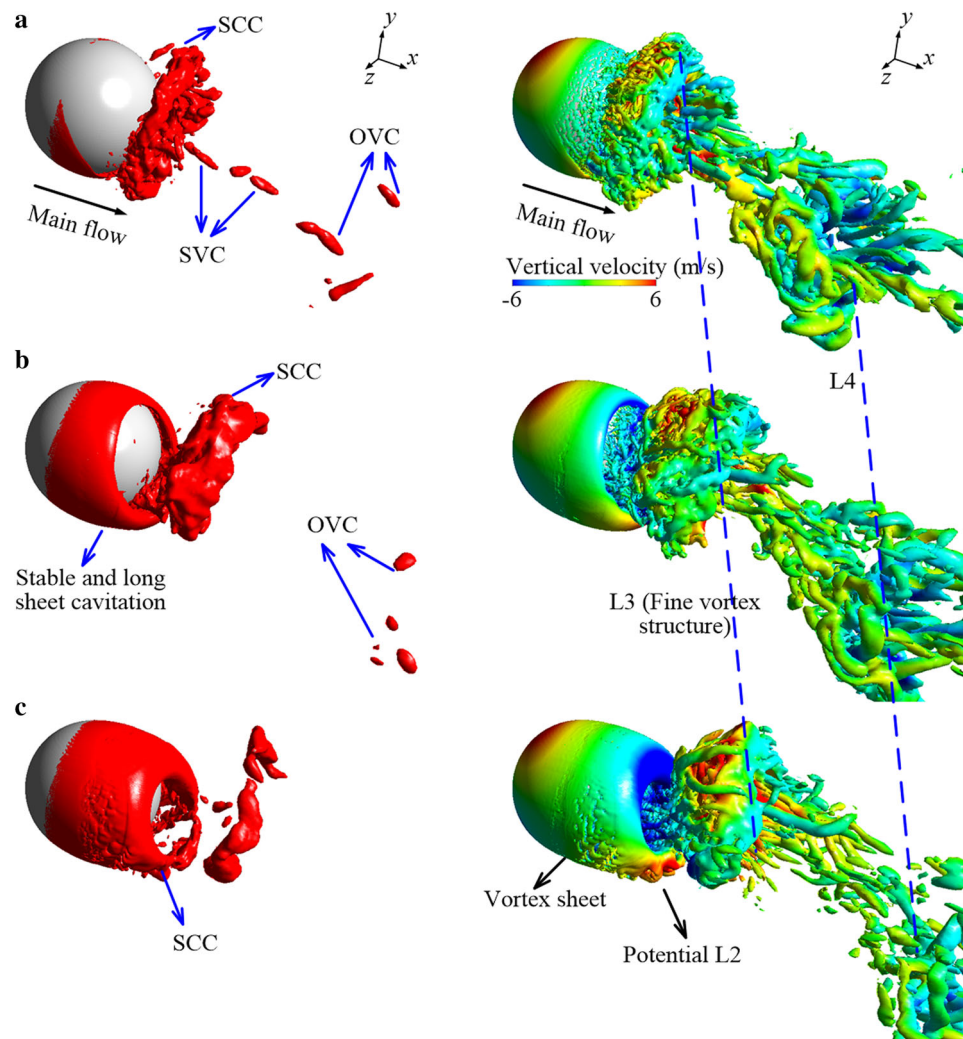


Fig. 15 Evolution of the transient cavitation and vortical structures in cycle B, **a** $T_0/6$, **b** $3T_0/6$, **c** $5T_0/6$ (left: cavity patterns given by isosurface $\alpha_v = 0.1$; right: vortical structures given by isosurface $Q = 20,000 \text{ s}^{-2}$). $\sigma = 0.75$, $Re = 1.5 \times 10^6$

ken cavitation structures developing from the SCC seen in part b_5 . It is noted that a very stable, long sheet cavitation continues to grow from b_1 to b_5 in cycle B that appears to not interact with the SCC. However these complex interactions between the shedding cloud cavitation and the newly growing sheet cavitation can be seen in cycles A and C.

The flow in cycle C in Fig. 16 starts from trough C marked in Fig. 11a, which is the local minimum with the highest St compared to those in troughs A and B. Cycle C in Fig. 16a shows a recently completed shedding of an oblique cavity and a HSVC forms in the wake following the SCC behind the lower surface. The OVC is observed in the far wake. These vortex cavitation structures (HSVC and OVC) are directly related to the vortex structures due

to the local low pressure in the vortex tubes. A new sheet cavitation forms and grows to nearly its largest length in Fig. 16b where a new SCC along the upper surface forms and the vortex cavitation structures (HSVC and OVC) are still apparent. In Fig. 16c, the HSVC breaks up into BVC at the far wake and the SVC can be clearly seen just behind the sphere. There is no new large-scale vortex forming from time points c_3 to c_5 with the newest vortex structures, L1, more likely being a sub-scale vortex structure like shown in Fig. 14.

These three types of vortex structures seem to alternately grow over time as shown by all the cycles in Fig. 11a. The transition from the fine vortex structure to the large-scale vortex structure seems to be a process that proceeds from energy preparation to release.

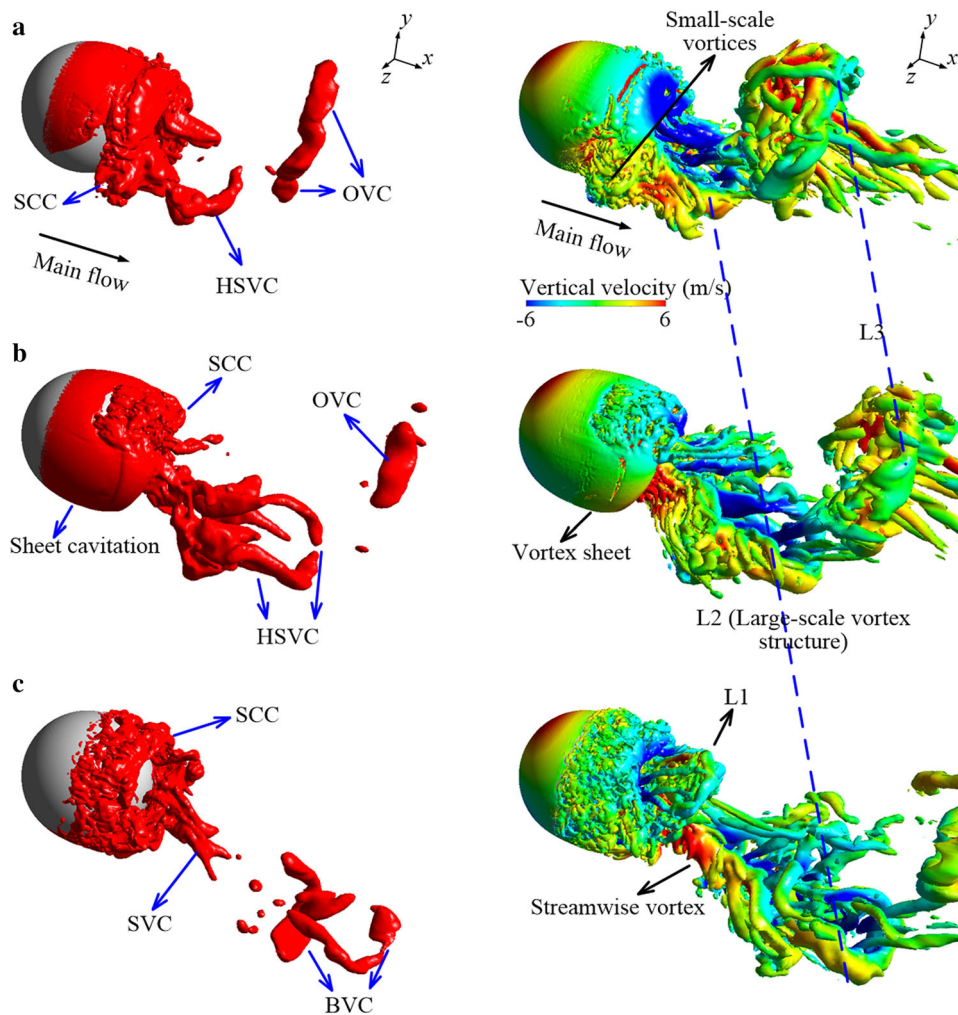


Fig. 16 Evolution of the transient cavitation and vortical structures in cycle C, **a** $T_0/6$, **b** $3T_0/6$, **c** $5T_0/6$ (left: cavity patterns given by isosurface $\alpha_v = 0.1$; right: vortical structures given by isosurface $Q = 20,000 \text{ s}^{-2}$). $\sigma = 0.75$, $Re = 1.5 \times 10^6$

4.6.2 Instantaneous vortex structures

The previous discussions showed the close relationship between the cavitation and the vortex structures, so these were investigated in detail to further understand the cavitation–vortex interactions. This section focuses on the instantaneous vortex structures while Sect. 4.5.3 focuses on the cavitation influence on the instantaneous vortices.

Figure 17 shows the three transverse planes used to show the velocity vectors and vorticity distributions (ω_x). Typical snapshots of the instantaneous vortex structures, velocity vector fields and vorticity distributions on these three planes are shown in Figs. 18, 19, 20 for cycles A, B and C. The sub-scale vortex structure and fine vortex structure are marked by the Q -criterion in Figs. 18 and 19. The velocity vectors in Figs. 18 and 19 show many clear vortices instead of the dominant large-scale vortex shown in Fig. 20. Plane $x/D = 2/3$ (Figs. 18c and 19c) has scattered patches of vorticity that

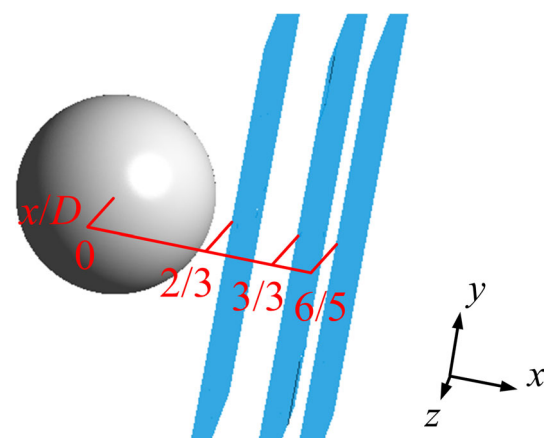


Fig. 17 Sketch of three transverse planes (y - z planes) at $x/D = 2/3$, $3/3$ and $6/5$ for showing the wake structures

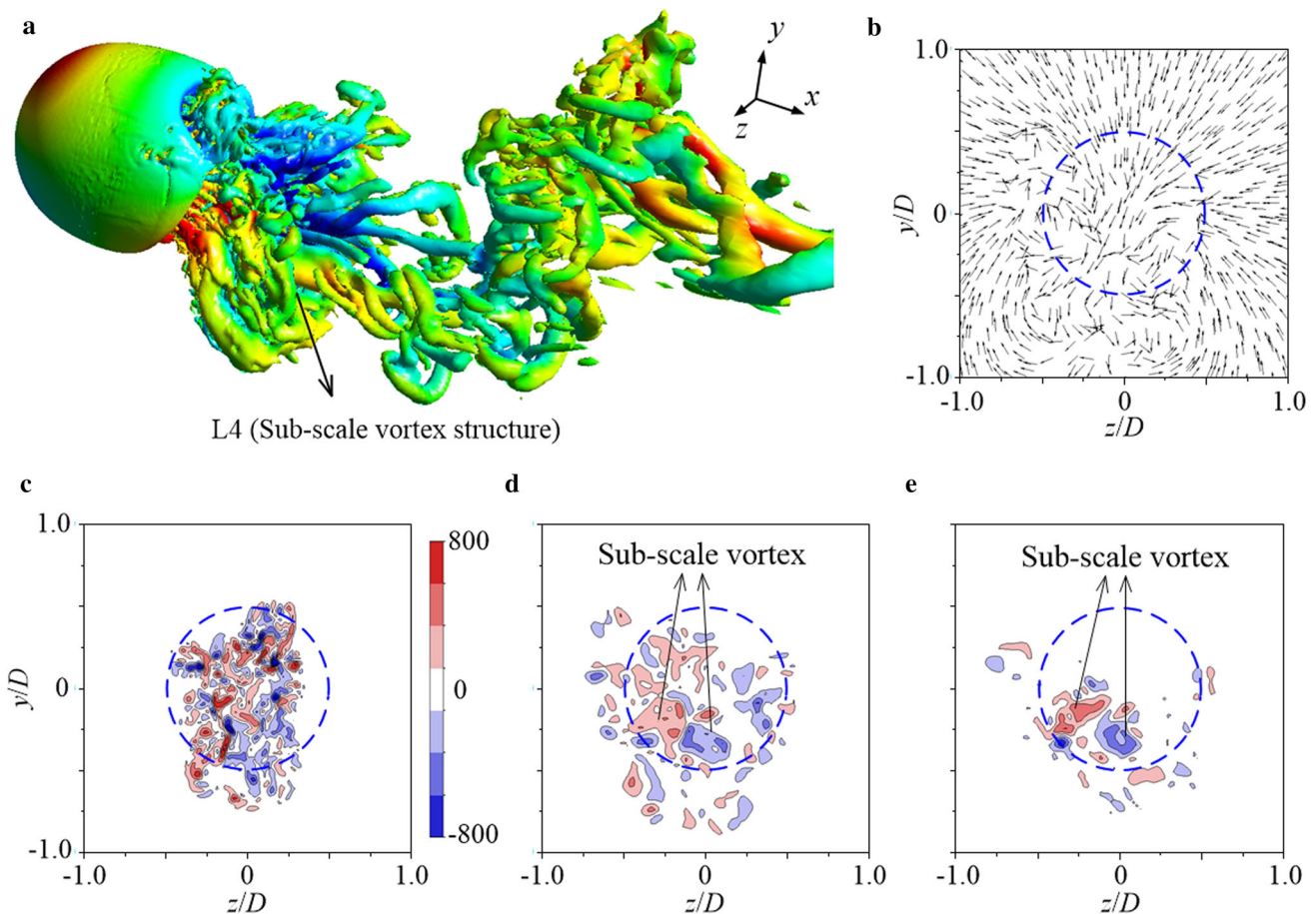


Fig. 18 **a** Instantaneous vortical structures, **b** velocity vectors at $x/D = 3/3$, **c** ω_x at $x/D = 2/3$, **d** ω_x at $x/D = 3/3$, and **e** ω_x at $x/D = 6/5$. $T_0/2$ in cycle A, $\sigma = 0.75$, $Re = 1.5 \times 10^6$ (The vortical structures are given by isosurface $Q = 20,000 \text{ s}^{-2}$. The blue dashed circle denotes the sphere body)

seem to correspond to the various small-scale vortices in the near field wake. Figure 18 shows two discernible vortices (i.e. the sub-scale vortex marked in Fig. 18a) that have relatively larger magnitudes than those in other regions. The surrounding small-scale vortices rapidly weaken with most no longer visible in Fig. 18e. Figure 19 shows the new vortex sheet growing as the previous vortex sheet sheds with numerous small-scale vortices forming in the near field wake. These small-scale vortices break down and rapidly weaken in the wake as shown in Fig. 19d, e.

In Fig. 20, the large-scale vortex with a horseshoe shape is clearly discernible. Two legs extend from the near the sphere and connect to each other with a downward facing head as shown in Fig. 20a. The roots of the two legs still connect tightly with the surrounding small-scale vortices which were shed from the vortex sheet. Two dominant counter-rotating vortices, i.e. the two legs of the large-scale vortex, are clearly shown in Fig. 20b. They drive the upper fluid to move downward between them. The near field wake has numerous small-scale vortices as shown in Fig. 20c, similar to cycle A and cycle B. However one large difference is that the vorticity

is divided into two main regions because of the influence of the large-scale vortex. This large-scale vortex finally sheds and is conveyed downstream. Some streamwise vortices that are rotating in opposite directions near the large-scale vortex are indicated in Fig. 20d, e.

4.6.3 Cavitation influence on the vortex in the sphere wake

The three cavitation shedding regimes discussed in Sect. 4.5.1 in Figs. 14, 15, 16 show that the vortex structures are clearly related to the cavitation. In Figs. 14 and 16, the sub-scale and large-scale vortex structures form due to the cloud cavitation shedding with the horseshoe-like shaped and horseshoe shaped cavitation structures (i.e. HLSVC and HSVC). The sheet cavitation sheds and breaks up into cavitating streak vortex filaments as shown in Fig. 14c, so the vortex sheet also breaks up into vortex filaments. These pictures illustrate that the main body of the vortex structure can be observed in the cavitation patterns. In Fig. 15, the previously shedding cloud cavitation has little influence on the growing sheet cavitation, so the stable vortex sheet becomes

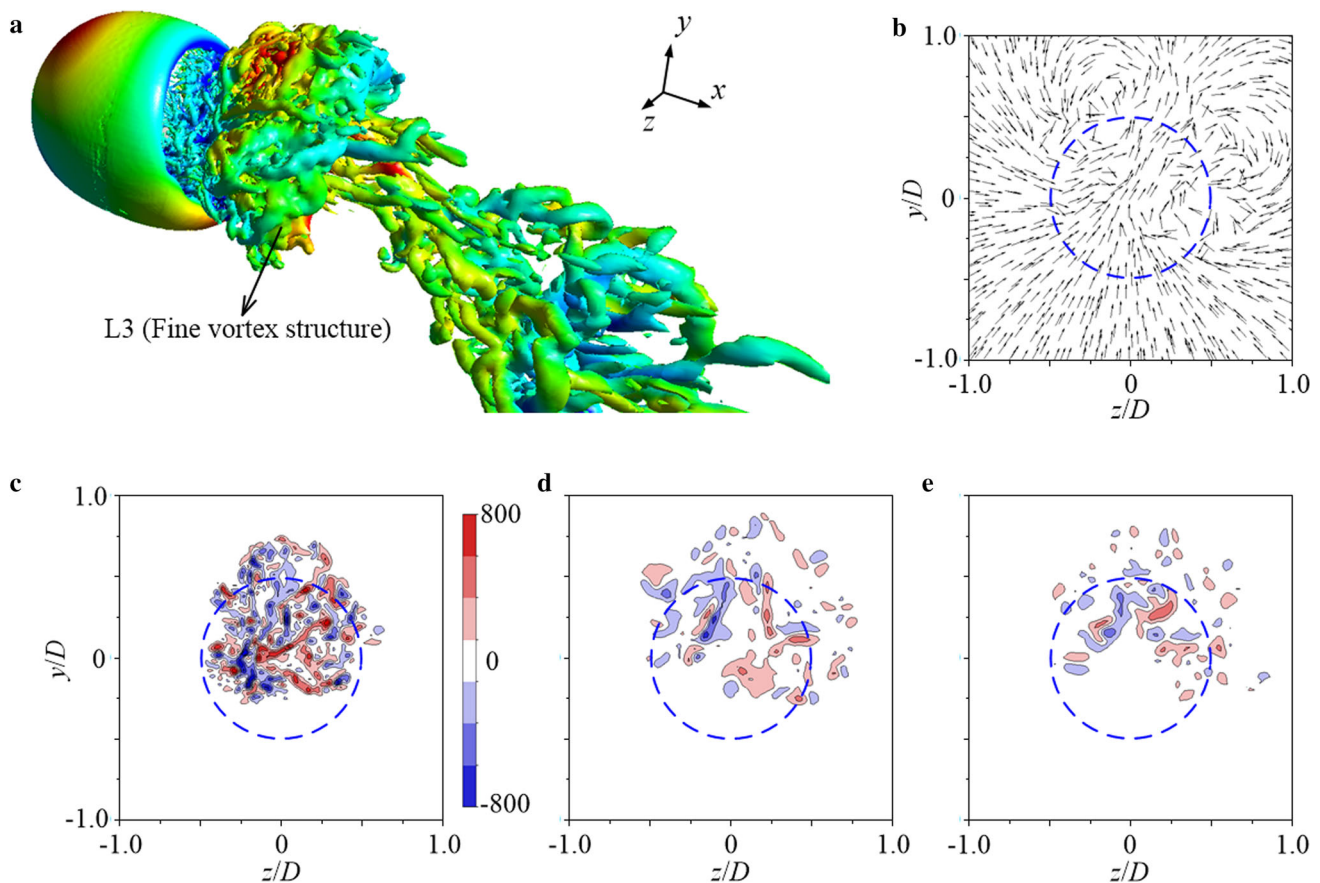


Fig. 19 **a** Instantaneous vortical structures, **b** velocity vectors at $x/D = 3/3$, **c** ω_x at $x/D = 2/3$, **d** ω_x at $x/D = 3/3$, and **e** ω_x at $x/D = 6/5$. $T_0/2$ in cycle B, $\sigma = 0.75$, $Re = 1.5 \times 10^6$ (The vortical structures are given by isosurface $Q = 20,000 \text{ s}^{-2}$. The blue dashed circle denotes the sphere body)

relatively long. The next shedding cloud cavitation starting from Fig. 15c contributes to a large-scale vortex structure which contains a large amount of energy and significantly influences the sphere wake.

The present numerical results clearly show the influence of the cavitation on the vortex. The effect of the cavitation on the vortex can be further quantified by the vorticity transport equation [18]. The vorticity transport equation in a variable density flow (e.g. a cavitating flow in this study) is

$$\frac{D\boldsymbol{\omega}}{Dt} = (\boldsymbol{\omega} \cdot \nabla)\mathbf{V} - \boldsymbol{\omega}(\nabla \cdot \mathbf{V}) + \frac{\nabla \rho_m \times \nabla p}{\rho_m^2} + (v_m + v_t)\nabla^2 \boldsymbol{\omega}, \quad (30)$$

where $D()/Dt$ denotes the material derivative and the four terms on the right hand side denote the vortex stretching term $((\boldsymbol{\omega} \cdot \nabla)\mathbf{V})$, i.e. the stretching and tilting due to the velocity gradients, the vortex dilatation term $(-\boldsymbol{\omega}(\nabla \cdot \mathbf{V}))$, i.e. the volumetric expansion/contraction, the baroclinic torque $(\frac{\nabla \rho_m \times \nabla p}{\rho_m^2})$, i.e. the misaligned pressure and density gradients) and the viscous diffusion $((v_m + v_t)\nabla^2 \boldsymbol{\omega})$, which is very small in high Reynolds number flows). The vorticity can be altered by the four terms on the right side.

Figure 21 shows the predicted transient vapor volume fraction, vorticity and the first three terms on the right side of the vorticity transport equation. The results are obtained at time point c_3 shown in Fig. 11b and it is a typical moment that includes three cavitation regions: region A (growing sheet cavitation on the lower sphere surface), region B (shedding cloud cavitation leaving the upper sphere surface), and region C (vortex cavitation in the sphere wake).

In region A, a new sheet cavitation grows longer into the wake. The vorticity in region A is positive and the magnitude is larger along the liquid–vapor surface than inside the sheet cavitation. The vortex stretching term is mainly important along the liquid–vapor surface where it is negative, which indicates that sheet cavitation with vapor formation reduces the vortex stretching term as also shown by Dittakavi et al. [18]. The vortex dilatation term significantly increases the vorticity along the liquid–vapor surface, but then reduces the vorticity inside the cavitation region.

The shedding cloud cavitation and the vortex cavitation are clearly discernible in regions B and C. A large amount of vorticity is generated by the cloud cavitation and the vortex cavitation. The vortex stretching term has dominant posi-

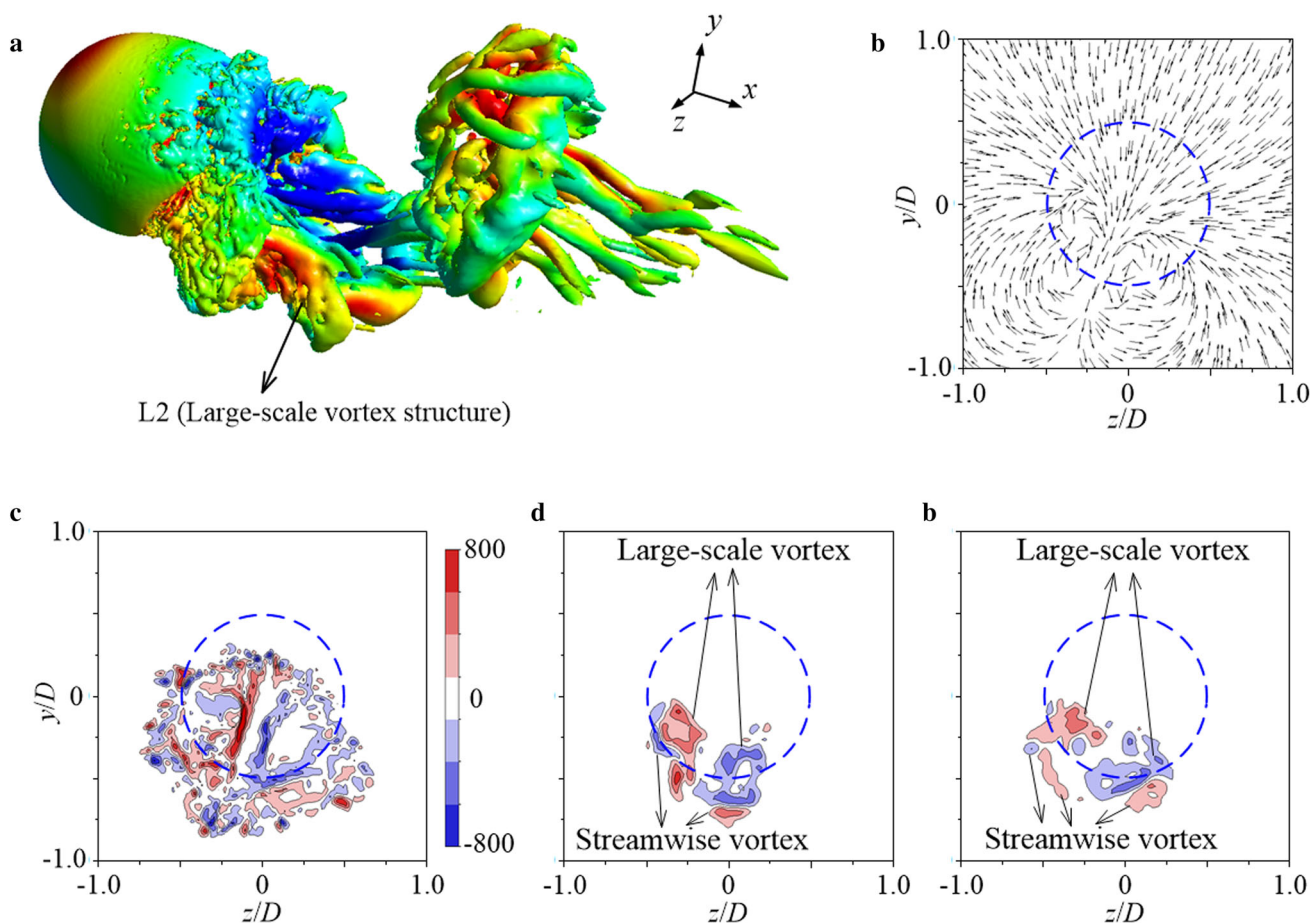


Fig. 20 **a** Instantaneous vortical structures, **b** velocity vectors at $x/D = 3/3$, **c** ω_x at $x/D = 2/3$, **d** ω_x at $x/D = 3/3$, and **e** ω_x at $x/D = 6/5$. $T_0/2$ in cycle C, $\sigma = 0.75$, $Re = 1.5 \times 10^6$ (the vortical structures are given by isosurface $Q = 20,000 \text{ s}^{-2}$. The blue dashed circle denotes the sphere body)

tive magnitude in region B and right behind the sphere. In region C and in the far wake where the vortex structures exist in the upper-right part of the flow, the vortex stretching term significantly affects the vorticity. The vortex dilatation and the baroclinic torque significantly increase in the cloud cavitation region and near the outside of the vortex cavitation). Inside the vortex cavitation, the baroclinic torque is negligible, but the vortex dilatation is still large. The vortex dilatation strongly influences the vorticity generation inside the vortex cavitation due to the vapor formation in the vortex tube.

5 Conclusions

The LES was coupled with a homogenous cavitation model to simulate a cavitating flow around a sphere. The numerical results accurately reproduce the cavitating flow around the sphere with good agreement with experimental data for various cavitation numbers ($0.36 \leq \sigma \leq 0.9$). The simulations capture the dynamics of the cavity inception, growth and

oblique shedding due to the re-entrant jet. Mesh resolution investigation and LES V&V analysis have been conducted to make sure the reliability of simulation results. The results were then used to study the wake characteristics behind a sphere for typical cloud cavitation conditions. The main conclusions can be summarized as follow.

- (1) The spectral characteristics of the cavitating flow in the sphere at a typical cloud cavitation condition, $\sigma = 0.75$, can be divided into the periodic cavitation mode, the high Strouhal number mode and the low Strouhal number mode. The near field wake is characterized by the periodic cavitation mode which corresponds to a quasi-periodic process with cavity growing and contracting. The high Strouhal number mode mainly influences the middle part of the wake with relatively larger peak St due to the interactions between the shedding cloud cavitation and a newly growing sheet cavitation. The far field wake is dominated by the low Strouhal number mode due to the significant influence of the large-scale vortex structure.

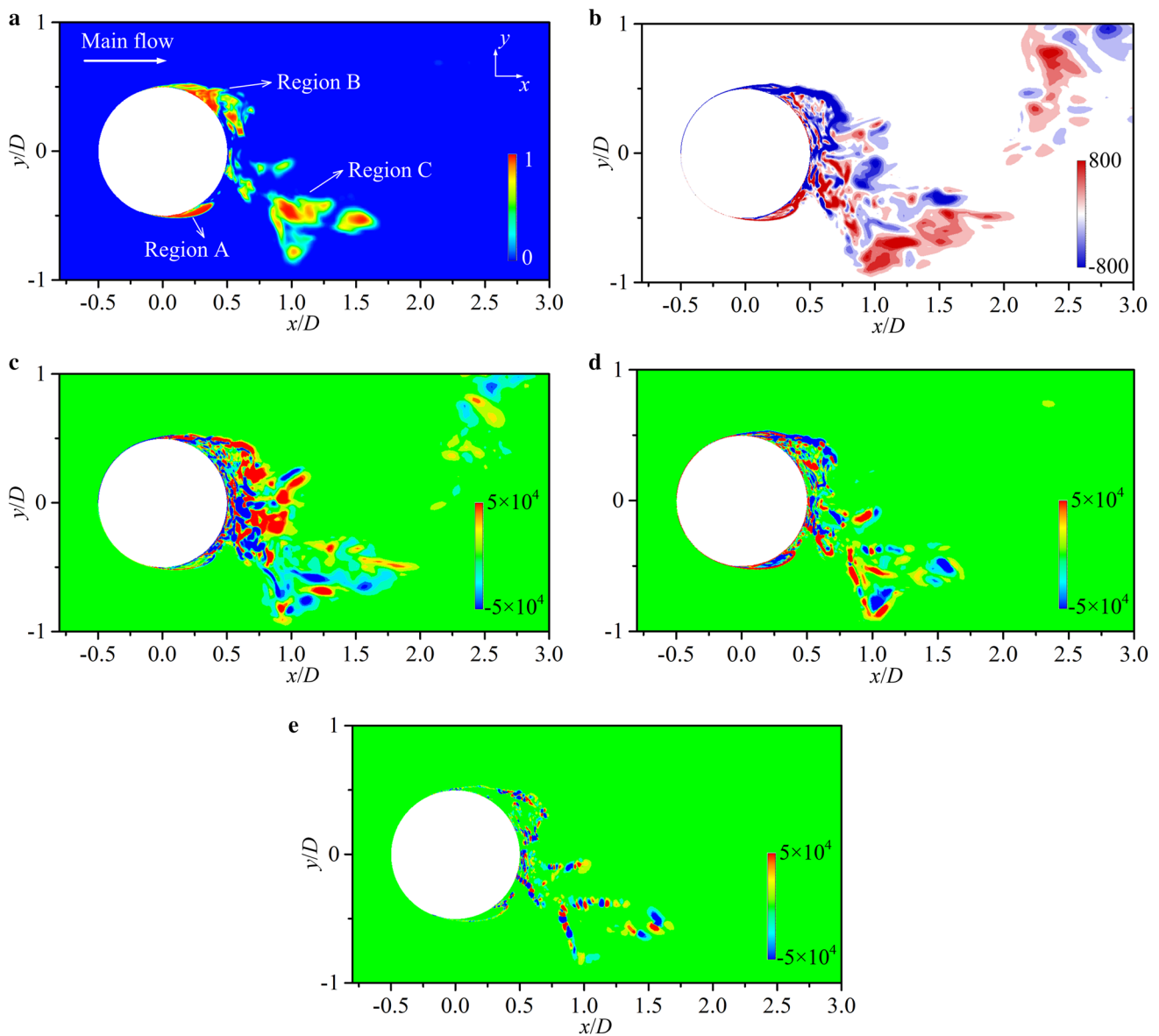


Fig. 21 Distributions of **a** vapor volume fraction, **b** vorticity (ω_z), **c** vortex stretching term, **d** vortex dilatation term, and **e** baroclinic torque. $\sigma = 0.75$, $Re = 1.5 \times 10^6$

- (2) Three cavity shedding regimes were observed with the formations of different vortex structures in the wake. Three main vortex structures, i.e. the sub-scale vortex, fine vortex structure and large-scale vortex, are clearly discernible in cycles A, B and C. In cycle A, the cavity shedding process produces the shedding cloud cavitation, the streamwise vortex cavitation and the horseshoe-like shaped vortex cavitation. In cycle B, cavity shedding leads to only simple cavitation structures and small-scale vortices instead of a relatively larger vortex structure. This regime did not show the interactions between the shedding cloud cavitation and the newly growing sheet cavitation. Cycle C included a clear large-scale vortex and the horseshoe shaped vortex cavitation.
- (3) The vortex structures are closely related to the cavitation evolution. The large-scale vortex, sub-scale vortex, streamwise vortex and many small-scale vortices are induced or influenced by the periodic cavity evolution. Analyses of the cavitation–vortex interactions indicate that the vortex structure formation is closely related to the shedding cloud cavitation. Analyses using the vorticity transport equation show that the vortex stretching term plays an important role in altering the vorticity in the sphere wake and that the vortex dilatation and baroclinic torque terms give a significant increase to the

vorticity at the cavitation closure region. In addition, the vortex dilatation strongly influences the vorticity generation inside the vortex cavitation due to vapor formation in the vortex tube.

Acknowledgements This work was financially supported by the National Natural Science Foundation of China (Grants 51822903 and 11772239) and the Natural Science Foundation of Hubei Province (Grant 2018CFA010). The numerical calculations were done on the supercomputing system in the Supercomputing Center of Wuhan University.

References

- Wang, G., Wu, Q., Huang, B.: Dynamics of cavitation–structure interaction. *Acta Mech. Sin.* **33**, 685–708 (2017)
- Luo, X., Ji, B., Tsujimoto, Y.: A review of cavitation in hydraulic machinery. *J. Hydrodyn. Ser. B* **28**, 335–358 (2016)
- Brandner, P.A., Walker, G.J., Niekamp, P.N., et al.: An experimental investigation of cloud cavitation about a sphere. *J. Fluid Mech.* **656**, 147–176 (2010)
- De Graaf, K.L., Brandner, P.A., Pearce, B.W.: Spectral content of cloud cavitation about a sphere. *J. Fluid Mech.* **812**, 1–13 (2017)
- Orley, F., Trummel, T., Hickel, S., et al.: Large-eddy simulation of cavitating nozzle flow and primary jet break-up. *Phys. Fluids* **27**, 086101 (2015)
- Yu, Z., Wang, G., Huang, B.: A cavitation model for computations of unsteady cavitating flows. *Acta Mech. Sin.* **32**, 273–283 (2016)
- Wei, Y., Tseng, C., Wang, G.: Turbulence and cavitation models for time-dependent turbulent cavitating flows. *Acta Mech. Sin.* **27**, 473–487 (2011)
- Arndt, R.E.A.: Cavitation in vortical flows. *Annu. Rev. Fluid Mech.* **34**, 143–175 (2002)
- Ganesh, H., Mäkiharju, S.A., Ceccio, S.L.: Bubbly shock propagation as a mechanism for sheet-to-cloud transition of partial cavities. *J. Fluid Mech.* **802**, 37–78 (2016)
- Hao, J.F., Zhang, M.D., Huang, X.: The influence of surface roughness on cloud cavitation flow around hydrofoils. *Acta Mech. Sin.* **34**, 10–21 (2018)
- Franc, J.P., Michel, J.M.: *Fundamentals of Cavitation*. Springer Science & Business Media, New York (2005)
- Kubota, A., Kato, H., Yamaguchi, H.: A new modeling of cavitating flows—a numerical study of unsteady cavitation on a hydrofoil section. *J. Fluid Mech.* **240**, 59–96 (1992)
- Gopalan, S., Katz, J.: Flow structure and modeling issues in the closure region of attached cavitation. *Phys. Fluids* **12**, 895–911 (2000)
- Wosnik, M., Qin, Q., Arndt, R.E.: Identification of large scale structures in the wake of cavitating hydrofoils using LES and time-resolved PIV. In: *Proceedings of 26th symposium on naval hydrodynamics*, Rome, September 17–22 (2006)
- Cheng, H.Y., Bai, X.R., Long, X.P., et al.: Large eddy simulation of the tip-leakage cavitating flow with an insight on how cavitation influences vorticity and turbulence. *Appl. Math. Model.* **77**, 788–809 (2020)
- Long, Y., Long, X.P., Ji, B., et al.: Verification and validation of large eddy simulation of attached cavitating flow around a Clark-Y hydrofoil. *Int. J. Multiphase Flow* **115**, 93–107 (2019)
- Budich, B., Schmidt, S.J., Adams, N.A.: Numerical simulation and analysis of condensation shocks in cavitating flow. *J. Fluid Mech.* **838**, 759–813 (2018)
- Dittakavi, N., Chunekar, A.R., Frankel, S.H.: Large eddy simulation of turbulent-cavitation interactions in a venturi nozzle. *ASME J. Fluids Eng.* **132**, 121301 (2010)
- Long, X., Zuo, D., Cheng, H., et al.: Large eddy simulation of the transient cavitating vortical flow in a jet pump with special emphasis on the unstable limited operation stage. *J. Hydrodyn. Ser. B* **32**, 345–360 (2020)
- Sakamoto, H., Haniu, H.: A study on vortex shedding from spheres in a uniform flow. *ASME J. Fluids Eng.* **112**, 386–392 (1990)
- Johnson, T.A., Patel, V.C.: Flow past a sphere up to a Reynolds number of 300. *J. Fluid Mech.* **378**, 19–70 (1999)
- Eshbal, L., Rinsky, V., David, T., et al.: Measurement of vortex shedding in the wake of a sphere at. *J. Fluid Mech.* **870**, 290–315 (2019)
- Cheng, X., Shao, X., Zhang, L.: The characteristics of unsteady cavitation around a sphere. *Phys. Fluids* **9821**, 042103 (2019)
- Pendar, M.R., Roohi, E.: Cavitation characteristics around a sphere: an LES investigation. *Int. J. Multiphase Flow* **98**, 1–23 (2018)
- Kolahan, A., Roohi, E., Pendar, M.: Wavelet analysis and frequency spectrum of cloud cavitation around a sphere. *Ocean Eng.* **182**, 235–247 (2019)
- Germano, M., Piomelli, U., Moin, P., et al.: A dynamic subgrid—scale eddy viscosity model. *Phys. Fluids* **3**, 1760–1765 (1991)
- Lilly, D.K.: A proposed modification of the Germano subgrid—scale closure method. *Phys. Fluids* **4**, 633–635 (1992)
- Zwart, P.J., Gerber, A.G., Belamri, T.: A two-phase flow model for predicting cavitation dynamics. In: *Proceedings of ICMF 2004 International Conference on Multiphase Flow*, Yokohama, June 1–3 (2004)
- Wu, Q., Huang, B., Wang, G., et al.: The transient characteristics of cloud cavitating flow over a flexible hydrofoil. *Int. J. Multiphase Flow* **99**, 162–173 (2018)
- Huang, B., Young, Y.L., Wang, G., et al.: Combined experimental and computational investigation of unsteady structure of sheet/cloud cavitation. *ASME J. Fluids Eng.* **135**, 071301 (2013)
- Oberkampf, W.L., Roy, C.J.: *Verification and Validation in Scientific Computing*. Cambridge University Press, Cambridge (2010)
- Brandner, P.A., Walker, G.J., Niekamp, P.N., et al.: Global mode visualisation in cavitating flows. In: *Proceedings of 16 h Australasian Fluid Mechanics Conference*, Crown Plaza, December 2–7 (2007)
- Venning, J.A., Giosio, D.R., Pearce, B.W., et al.: Global mode visualisation in cavitating flows. In: *Proceedings of 10th International Symposium on Cavitation*, Baltimore, May 14–16 (2018)
- Bakic, V., Peric, M.: Visualization of flow around a sphere for reynolds numbers between 22000 and 400000. *Thermophys. Aeromech.* **12**, 307–315 (2005)